Characterization of a latent thermal energy storage heat exchanger using a charging time energy fraction method with a heat loss model

Kenny Couvreur[a], Wim Beyne[a], Robin Tassenoy[a], Steven Lecompte[a], Michel de Paepe[a,b]

[a] Department of Electromechanical, Systems and Metal Engineering, UGent, Ghent, Belgium.
[b] FlandersMake@UGent – Core lab EEDT-MP, Leuven, Belgium

Abstract

Correlations predicting the transient behavior of latent heat thermal energy storage systems without too many computational efforts are valuable for engineering practices. This characterization of latent heat thermal energy storage systems can be done with the recently developed charging time energy fraction method. This method allows fitting a predictive model for the outlet heat transfer fluid temperature of a latent thermal storage unit as a function of the input condition. The previous application of the method neglected heat transfer to the ambient. The present paper improves the charging time energy fraction method by proposing a heat loss model to the charging time energy fraction model. A finite volume model of a high-temperature thermal battery is used to validate the proposed heat loss model. The improved charging time energy fraction method is then used to characterize a high-temperature thermal battery by calibrating a model on 36 numerical charging experiments. The charging time prediction between energy fractions of 0 and 0.96 deviates maximally 2 % from the measured charging time over all 36 calibration experiments. The deviation increases near the end of the charging process, especially for slower charging experiments. Across the 36 calibration experiments, the worst prediction has an average absolute temperature difference of 0.50 °C with a maximum deviation of 2.58 °C at the very beginning of the charging where fast transients are occurring. The calibrated model is also compared to four numerical validation experiments and four real experiments. Overall it is shown that this low computational cost model with average calculation times of 2-3 ms can accurately predict the heat transfer fluid outlet temperature of latent thermal energy storage heat exchangers.

Keywords

Latent thermal energy storage characterization; charging time energy fraction method; Finned shell and tube heat exchanger, Experimental predictive model, Heat loss model; Model validation

1 Introduction

Recently, in December 2019, the European Commission presented the “European Green Deal”, a set of policy initiatives aiming at ensuring the EU becomes climate neutral by 2050, implying a significant acceleration of emission reductions [1]. Therefore the European Commission underlines the importance of increasing energy efficiency and increasing the share of renewable energy resources to fulfill our energy demand [2]. The deployment of renewable energy, which mainly comes from solar and wind entails also some problems. Due to the periodic nature of solar energy and the intermittent availability of wind energy, energy storage becomes necessary to increase the share of renewables in our energy market. This is also recognized by the European Commission which stresses the essential role of storage in achieving the EU’s greenhouse gas emission reduction targets. Large-scale electrical energy storage and hydrogen storage are given great potential [3, 4]. The role of thermal energy storage remained initially underexposed as a potential technology in the EU’s energy transition [5, 6] but more initiatives are taken with specific research programs on thermal storage for decarbonizing buildings, high-temperature thermal storage for industrial processes and thermal storage for power-to-heat-to-power technology [7].

Since the 1980s there is an increasing research effort into thermal storage units that utilize the latent heat of materials, the so-called phase changing materials (PCMs) because they offer advantages over materials whose thermal storage capacity is exclusively based on sensible heat [8-11]. Latent heat energy storage (LHES) or latent heat thermal energy storage (LHTES) or latent thermal energy storage (LTES) is considered a crucial energy technology by creating compact and efficient thermal energy storage units, which are highly desirable in our current and future energy market for increased use and integration of renewable energy systems and to pursue carbon neutrality [12-15]. Despite the potential and the long research history, LTES systems are neither widespread in the energy market, nor in residential applications and in industrial processes. This is partially attributed to the difficulties in designing LTES units and predicting their performance [16, 17]. Other drawbacks are the poor thermal conductivity of common PCMs [18-20].

The further development of an LTES system involves the understanding of two essentially diverse subjects: PCMs and heat exchangers. The choice of PCMs in the appropriate temperature range requires knowledge of the thermophysical property data, melting and freezing characteristics, short-term and long-term behavior, material compatibility, and long-life stability considerations [18, 21]. Several solutions to overcome the poor thermal conductivity of common PCMs have been investigated through enhancement of the heat transfer rate within PCMs as discussed in multiple review papers [22-24]. Generally, the enhancement techniques are classified according to the addition of high thermal conductivity additives such as nanoparticles [25] or high thermal conductivity matrices such as metal foam , or graphite, (micro)encapsulation of PCMs or the utilization of extended surfaces such as radial and longitudinal fins [26].

Compared to the use of highly conductive matrices or particle dispersion techniques extended surfaces have the benefits of ease of installation and require less maintenance during operation [27]. Extensive work has been done to improve the geometries of these extended surfaces to increase the LTES performance. Helical or spiral fin structures have been investigated by Zhang et al. [28], Duan et al. [29], Mehta et al [30] and Lu et al [31]. In the work of Sciacovelli and Verda [27], Johnson et al. [32, 33] or Zhang and Chen [34] tree-shaped fins are studied. Sheikholeslami et al. optimized the fin configuration of a snowflake-shaped fin with a finite element method [35, 36]. More nature-inspired configurations can also be found in the work of Wu et al. who numerically studied a spiderweb-like structure to improve the discharging efficiency [37]. All these studies have in common that the fin

shape is optimized to create a better temperature uniformity and hence faster charging or discharging rates and overcome the poor thermal conductivity of PCMs.

Besides the creation of these complex fin geometries, research on the more classical fin structures like the plain longitudinal fins and annular fins is still ongoing. This mainly relates to studying the effect of different fin heights, thickness, and numbers or orientation on the charging or discharging efficiency. Modi et al. analyzed this for a longitudinally finned tube horizontal LTES system [38]. Similar research can be found in the work of Mao et al. on a vertically oriented LTES unit with a novel longitudinal fin design [39]. Yang et al. study the optimal number of longitudinal fins in a horizontal finned LTES unit [40]. For annular fin structures the size and distribution is analyzed by Yang et al. [41]. Zhu and Qiu also studied the role of annular fins [42]. Not only is the fin size and distribution an important aspect, also the orientation of fins has a noticeable effect on the heat transfer. Guo et al. showed that the heat transfer rate can be increased for angled annular fins compared to horizontally placed fins [43]. The influence of fin parameters on the thermal performance of conical shell and tube LTES unit has been investigated by Kalapala and Devanuri [44].

These studies show that the heat transfer problems in PCMs are complicated and characterization of a specific LTES design is not straightforward. This is because heat transfer in PCM storages is a transient and non-linear phenomenon with a moving solid–liquid interface [45, 46]. Although understanding of the fundamentals of melting and solidifications in representative units of a complete heat exchanger is necessary, the deployment of LTES systems in energy systems relies on further research on efficient and accurate characterization methods. In a recent book chapter on the design of LTES systems, Groulx et al. [47] highlighted the necessity of high quality experiments on LTES systems and testing it with the appropriate process conditions. Indeed, testing complete LTES heat exchangers is required to determine the performance of a storage system since performance of a LTES heat exchanger cannot be predicted based on the characterized representative units [48]. This has resulted in a large amount of research testing specific heat exchangers reporting either graphs of the LTES thermal performance or performance indicators for a number of operating conditions [49-56].

Therefore, physically representative models are required to predict and evaluate the performance of a LTES heat exchanger not restricted to a limited number of operational conditions. One of the most common model type are numerical models relying on the discretization of the conservation laws. In the previously mentioned research on heat transfer enhancement these type of models are mostly used and have been reviewed by for example Verma et al., Al-abidi et al. and Dutil et al. [57-59]. These models can be further split in those ignoring natural convection in the PCM often using a self-developed program [60, 61] and CFD models deployed in ANSYS Fluent or COMSOL Multiphysics software [56, 58, 62]. Both types allow to determine the thermal response for specific input conditions and characterize the LTES system. However, full CFD simulations are rarely appropriate due to their complexity and computational cost. Moreover, often factors such as the mushy zone constant [56, 63-66] are needed to accurately describe the phase change process or natural convection Nusselt correlations are used [67] which require fitting to experimental results. The computational time required for these models can make this fitting unfeasible for full heat exchangers and therefore CFD results are often reduced to an overall heat transfer coefficient [54, 68, 69], which in combination with effectiveness-number of transfer units (ε-NTU) or logarithmic mean temperature (LMTD) method provide a model for the LTES heat exchanger.

ε-NTU and LMTD methods are widely used methodologies in the design and evaluation of heat exchangers [70]. However, these methods are not directly applicable to LTES heat exchangers since they are based on the assumption of a heat exchanger in steady-state [70]. During charging or discharging, the internal energy of a LTES heat exchanger changes with time and therefore does not

operate in steady state. This transient behavior of a LTES unit is then sometimes overly simplified and a constant NTU is considered [71, 72] or an average effectiveness together with a variable NTU is used to give an indication of the performance of the LTES unit [73]. The ε-NTU method thus only enables to give the average heat transfer rate and phase change time over the phase change process but does not lead to a full characterization [55].

Researchers also tend to look for simplified (approximate) analytical models characterizing a specific geometry. Zhao et al. reviewed analytical studies of melting rate enhancement with fin and/or foam inserts [74]. Typically, an analytical expression is derived for the PCM temperature distribution [75], fin temperature distribution [76, 77], the melt fraction [78, 79] or the phase change front location [77, 79, 80] as function of time. These expressions are generally developed under the assumption of an isothermally heated wall and thus only characterize a small part of a full LTES heat exchanger where the HTF temperature is variable in time and space. Bauer used an effective medium method to predict the solidification times of macroscopic finned-PCM systems [81] and is also used by Tarragona et al. [82]. Fornarelli et al. developed a simple model for the total melting time considering an averaged constant heat transfer coefficient between the uniformly heated wall at constant temperature and the PCM [83]. Next to studies giving a theoretical framework for the derivation of the total phase change time expressions, there are also studies which reduce the results obtained from experiments [52, 84] or numerical experiments [85, 86] for a given geometry to a correlation of the phase change time.

In these approximate analytical models the heat transferred to or from the PCM is considered the sum of three contributions: sensible heating (or cooling) of the solid PCM, phase change and sensible heating (or cooling) of the liquid PCM. At each point in time there is either a combination of at least two contributions or a single contribution (which is mostly in the beginning and near the end of a process). Predicting the distribution among these contributions is difficult. Integration of these three contributions from a uniform starting condition ($t = 0$) to a uniform end condition ($t = t_{end}$) however simplifies the calculation procedure and forms the basis of most analytical derivations of the total phase change time. What happens in between time $t = 0$ and the total phase change time, $t = t_{end}$ is not defined. Therefore these total phase change time correlations only give the average heat transfer rate.

It is clear that these models or correlations expressing the total charging time or phase change time are thus not able to characterize a full heat exchanger and predict the outlet state as function of time. Correlations predicting the transient behavior of LTES devices are considered more valuable than those predicting endpoint phase change time and therefore only the average heat transfer rate for a given storage capacity. In light of these problems the absence of design or characterization methods is often recognized but limited progress is reported. Instead researchers focus on for example improving computational efforts or accuracy rather than proposing a new method [87].
Until recently, there was no general method available to obtain a predictive model for key performance indicators based on experimental data. As a result, comparing results of studies executed with different operational points (inlet mass flow rate and temperature) was difficult. Therefore, each specific LTES heat exchanger had to be tested again for each new application. The recently developed charging time energy fraction method (CTEFM) [17] provides a method for characterizing the outlet temperature of a LTES heat exchanger as a function of the heat transfer fluid (HTF) inlet conditions and initial condition. The CTEFM allows to reduce the results from experimental data and derive a model for the charging time, t_c as function of the energy fraction, α as shown in Figure 1. Reformulating this correlation to stored energy as function of time and differentiating this allows to retrieve the efflux of energy and eventually the outlet state of the HTF.

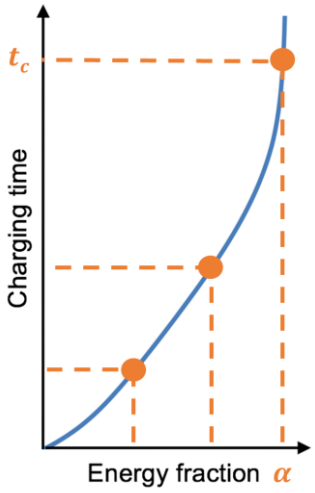

Figure 1. The CTEFM allows to retrieve charging time – energy fraction correlation of a LTES heat exchanger

However, the assumptions used to derive the CTEFM does not consider heat losses. Therefore, the present paper further develops the charging time energy fraction method by adding heat transfer to the ambient to the model. In Section 2, the charging time energy fraction method is introduced and the required adaptations to the charging time energy fraction method are explained. In Section 3, a high-temperature LTES heat exchanger is introduced as a test case for the CTEFM adaptations. The experimental set-up used is described and the experimental results are briefly discussed. Only a limited set of four experiments could be performed and experimental techniques are not sufficient to validate the proposed CTEF heat loss model. Therefore, Section 4 develops a finite volume model of the LTES heat exchanger. The fitting procedure is explained and the model is validated against the set of four experiments. Section 5 discusses the CTEF model calibration. The finite volume model is used to generate the data required to calibrate the novel charging time energy fraction method. Eventually Section 6 discusses the evaluation of the CTEF model. A flowchart of this working methodology is inserted in Appendix C.

2 Charging time energy fraction method

The CTEF method is a method to derive a low computational cost model based on a set of experiments which predicts the outlet temperature of a LTES heat exchanger for a given constant heat transfer fluid (HTF) inlet temperature and mass flow rate [17].

2.1 Charging time energy fraction model

The method is based on an idealized charging cycle where the LTES heat exchanger initial state is known. A HTF flow with constant mass flow rate and inlet temperature is applied. Heat transfer to the ambient is neglected and as a result the total internal energy change of the LTES heat exchanger, ΔU can be determined based on the initial state, the inlet temperature of the HTF and the material properties of PCM, container and HTF (Eq. 1).

$$\Delta U = U\left(T_{HTF,in}\right) - U\left(T_{LTES,ini}\right) \quad 1$$

As outlined in the work of Beyne et al. [17], for an adiabatic system the stored internal energy at any time during the charging cycle $J(t)$ can be written as Eq. 2 with $\alpha(t)$ the energy fraction as function

of time. This energy fraction is a continuously increasing function between 0 and 1. It is thus a cumulative distribution function describing the stored energy.

$$J(t) = \int_{t_{start}}^{t} dU = \alpha(t)\,\Delta U \tag{2}$$

If heat transfer to the ambient, $\dot{Q}_{loss}$ is neglectable, the stored internal energy change $J(t)$ is equal to the integrated efflux of energy $F(t)$ (Eq. 3 and Eq. 4). The integrated efflux of energy can be determined based on the energy fraction $\alpha(t)$ and the efflux of energy can be resolved to the outlet state for a given inlet mass flow rate and state. The charging time energy fraction method is based on predicting the energy fraction as a function of time and using it to determine the efflux of energy.

$$F(t) = \int_{t_{start}}^{t} \dot{m}(t)\big(h_{in}(t) - h_{out}(t)\big)\,dt \tag{3}$$

$$F(t) = \alpha(t)\Delta U \quad , \qquad if\ \dot{Q}_{loss} = 0 \tag{4}$$

Instead of correlating the energy fraction as a function of time, Beyne et al. [12] correlate the time required to reach a specific value of the energy fraction (Eq. 5)

$$t_c(\alpha_i) = t\ for\ which\ \alpha(t) = \alpha_i \tag{5}$$

The correlation proposed to construct the charging time energy fraction method is an expansion of an analytical solution for the total phase change time by Bauer et al. [81] which was extended for the total charging time of a full heat exchanger by Beyne et al. [12]. The general correlation for the total charging time is in the form of Eq. 6 where ΔT is the temperature difference between the HTF inlet temperature and the PCM phase change temperature.

$$t_c = \frac{slope}{\Delta T} + intercept \tag{6}$$

The structure of the *slope* is based on the correlations proposed in Bauer et al. [88] but a general correlation for both *slope* and *intercept* are lacking. Hence, the *slope* and *intercept* have to be fitted for each specific LTES heat exchanger separately to construct the charging time energy fraction model. This fitting process is described by Beyne et al. [17] where both the *slope* and the *intercept* are functions of the HTF mass flow rate, $\dot{m}$. The inlet temperatures should be chosen in such a way that $\frac{1}{\Delta T}$ is equally distributed. Consequently, the best fitting of parameters *Slope* and *Intercept* would be possible.

The charging time correlation used to estimate the efflux of energy and HTF outlet temperature is thus given by Eq. 7 with *A, B, C,* and *D* fitting coefficients.

$$t_c(\alpha) = \left(A(\alpha) + \frac{B(\alpha)}{\dot{m}}\right)\frac{1}{\Delta T} + \left(C(\alpha) + \frac{D(\alpha)}{\dot{m}}\right) \tag{7}$$

By determining the *A, B, C* and *D* coefficients for a set of energy fractions, the charging time is estimated in a set of discrete points. The charging time can be inverted to determine the energy fraction which in term allows to predict the integrated efflux of energy through Eq. 4 . Through

differentiation of the integrated efflux of energy, the efflux of energy is obtained which can then be resolved for the HTF outlet temperature.

The charging time energy fraction method developed by Beyne et al. [17] is based on the assumption there is no heat transfer to the ambient. There are two major adaptations required in order to include heat losses into the charging time energy fraction method. Firstly, the efflux of energy is now equal to the sum of the internal energy change and the heat transfer to the ambient (Eq. 8). These heat losses thus need to be estimated. Secondly, for an ideal infinite charging cycle, the LTES heat exchanger does not reach the inlet temperature of the HTF. The energy fraction thus does not reach a value of one.

$$F(t) = \alpha(t)\Delta U + Q_{loss}(t) \quad 8$$

The modification required to the CTEFM is shown with the help of a graphical representation on Figure 2. The y-axis is the integrated efflux of energy over the maximal stored energy. The full black line represents the integrated efflux of energy, $F(t)$ which consists of a part stored internal energy, $J(t)$ and the integrated losses, $Q_{loss}(t)$. Due to the losses this curve could potentially exceed the threshold value of one which is the maximum possible energy fraction indicated by the horizontal dashed line. The CTEFM requires knowledge of the evolution of the energy fraction over time. Therefore a heat loss model is necessary to account for integrated losses and obtain the blue curve on Figure 2 which is the energy fraction $\alpha(t)$.

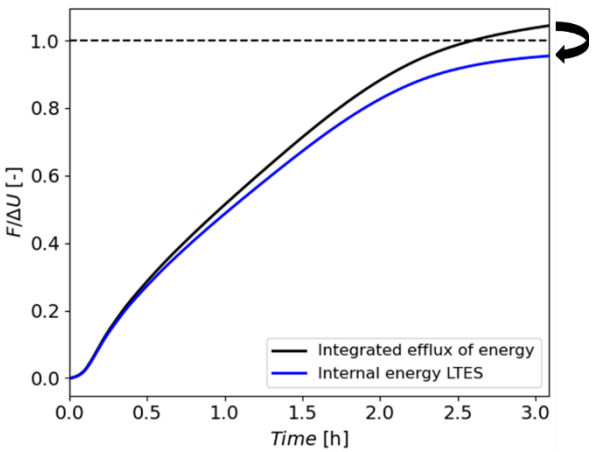

Figure 2. Graphical representation of the modification required to use the CTEFM when heat losses are present in a LTES system.

2.2 Addition of a heat loss model

The charging time energy fraction method requires correlating the energy fraction $\alpha(t)$ to predict the outlet state of the LTES heat exchanger. If for an adiabatic system this can be done as in Eq. 4, for a system with heat losses this reads as Eq. 9, with $Q_{loss}(t)$ the integrated heat losses as in Eq. 10.

$$\alpha(t) = \frac{1}{\Delta U}(F(t) - Q_{loss}(t)) \quad 9$$

$$Q_{loss}(t) = \int_{t_{start}}^{t} \dot{Q}_{loss}(t)dt \quad 10$$

Eq. 9 can be rewritten as Eq. 11 by differentiating the energy fraction function $\alpha(t)$ with respect to time which is the basis of the CTEF heat loss model.

$$\frac{d\alpha(t)}{dt} = \frac{1}{\Delta U}\left(\frac{dF(t)}{dt} - \dot{Q}_{loss}(t)\right) \quad 11$$

Heat losses from a system can also be described by the overall heat transfer coefficient, UA_{loss}, if assumed independent of the battery surface temperature. This is graphically shown in Figure 3. Heat is lost from the LTES system to the environment at a certain temperature T_{amb}. The LTES system has a number of constituents (HTF, tube wall, PCM, insulation) each at a certain temperature. The internal energy of the LTES heat exchanger U can be determined as the sum of the internal energy of the PCM U_{PCM}, container U_{cont} and HTF U_{HTF} as a function of the local state of the LTES heat exchanger. The insulation is not considered to contribute to the internal energy change of the LTES heat exchanger and the internal energy change of the insulation is accounted for in the heat losses. Therefore, the heat losses can be modelled as Eq. 12 where $T_{surf,1}(t)$ is the LTES heat exchanger surface temperature.

$$\dot{Q}_{loss}(t) = UA_{loss}(T_{surf,1}(t) - T_{amb}) \quad 12$$

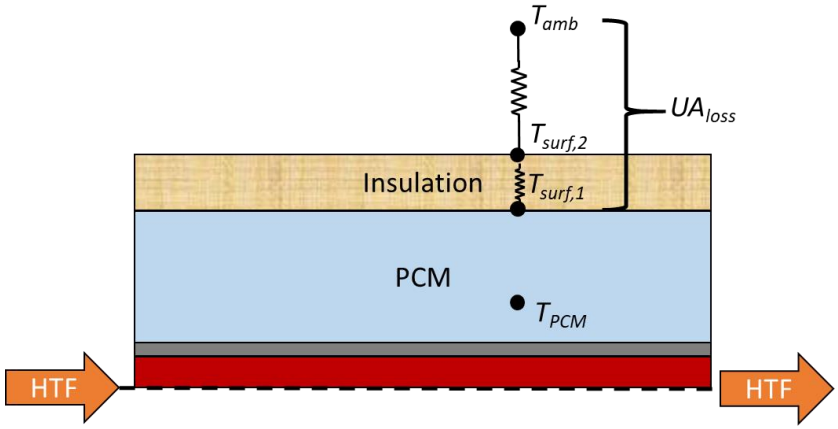

Figure 3. Representation of the considered LTES system as one tube. Between the PCM and ambient a heat loss factor is assumed which requires fitting to experimental data.

Combining Eq. 11 with Eq. 12 gives Eq. 13.

$$\frac{d\alpha(t)}{dt} = \frac{1}{\Delta U}\left(\frac{dF(t)}{dt} - UA_{loss}(T_{surf,1}(t) - T_{amb})\right) \quad 13$$

If the surface temperature $T_{surf,1}(t)$ can be written as a function of the energy fraction, α, Eq. 13 can be resolved as an ordinary differential equation with the integrated efflux of energy determined from the experimental data. Therefore, Eq. 14 is proposed to describe the LTES container surface temperature, $T_{surf,1}$ as function of the energy fraction, α.

$$T_{surf,1}(t) = T_{ini} + f(\alpha)\left(T_{HTF,in} - T_{ini}\right) \quad 14$$

The surface temperature should be in between the initial uniform starting temperature of the LTES, T_{ini} and the HTF inlet temperature, $T_{HTF,in}$, during the charging cycle. Therefore the function $f(\alpha)$ needs to be continuously increasing. A power law is proposed as Eq. 15 with the exponent value *n,* any positive real number. This function then determines how the surface temperature evolves between the initial starting temperature and the HTF inlet temperature. A more complex function can be proposed which more accurately describes the surface temperature as function of the energy fraction. However, this would increase the number of parameters to fit. The exponent *n* and overall heat loss coefficient, UA_{loss} are fitted together based on the measured heat losses. Through this

combined parameter fitting a function accurately describing the surface temperature is not strictly necessary as a deviation in surface temperature will be balanced by a change in UA_{loss}. As such, within the experimental uncertainties present a unique solution thus does not exist. Moreover, as the heat losses only tend to contribute to a minor extent to the total energy balance, deviations in the heat loss prediction will not be detrimental to the prediction of the energy fraction over time. Therefore increasing the complexity of the function does not lead to a significant reduction in fitting error compared to the measurement error and Equation 15 is retained to describe the surface temperature.

$$f(\alpha) = \alpha(t)^n \tag{15}$$

Combining Eq. 13, 14 and 15 results in Eq. 16 which represents the CTEF heat loss model.

$$\frac{d\alpha(t)}{dt} = \frac{1}{\Delta U}\left(\frac{dF(t)}{dt} - UA_{loss}\left(T_{ini} + \alpha(t)^n\left(T_{HTF,in} - T_{ini}\right) - T_{amb}\right)\right) \tag{16}$$

This ordinary differential equation can be solved for $\alpha(t)$ if UA_{loss} and the power factor n are known. The overall UA_{loss} and power factor *n* are characteristic values for the LTES heat exchanger and should be fitted to the experimental results. Fitting UA_{loss} and *n* requires an objective function.

During an ideal charging process of an adiabatic system with a constant HTF inlet temperature and HTF mass flow rate, the HTF outlet temperature will eventually approach the HTF inlet temperature at the end of charging process. On the other hand when heat losses are present during the charging process, the efflux of energy equals the heat losses if the experiment is continued until a steady state is reached (Eq. 17).

$$\dot{F}(t_{end}) = \dot{Q}_{loss}(t_{end}) \tag{17}$$

At the end of a charging cycle when the internal energy of the LTES unit does not change any more $\frac{d\alpha(t)}{dt}$ equals zero. Besides, $\frac{dF(t)}{dt}$ equals the efflux of energy $\dot{F}(t)$ and is measured throughout the charging process. At the end of a charging cycle the efflux of energy $\dot{F}(t_{end})$ equals the heat losses $\dot{Q}_{loss}(t_{end})$ (Eq. 17). Also the energy fraction at the end of the charging cycle $\alpha(t_{end})$ can be retrieved from solving the CTEF heat loss model for $\alpha(t)$ (Eq. 16). These known states in fact simplify the fitting process as an objective function can be derived from Eq. 16 for time $t = t_{end}$, where $\frac{d\alpha(t)}{dt}$ equals zero. It only requires experimental data from multiple charging cycles with different inlet conditions. The objective function which determines the absolute difference between the efflux of energy $\dot{F}(t_{end})$ and the heat losses $\dot{Q}_{loss}(t_{end})$ is then minimized over a set of *j* experiments by varying the parameters UA_{loss} and n as in Eq. 18.

$$minimize \sum_{exp=i}^{j} \dot{F}(t_{end}) - UA_{loss}\left(T_{ini} + \alpha(t_{end})^n\left(T_{HTF,in} - T_{ini}\right) - T_{amb}\right) \tag{18}$$

Once the overall heat loss UA_{loss} and power factor *n* are determined, Eq. 16 is solved for $\alpha(t)$ for all experiments. The charging time energy fraction model is then applied as outlined in the work of Beyne et al. [17] where four coefficients are fitted to determine the charging time as a function of the energy fraction (Eq. 7).

With the inversion of the charging time in a set of discrete energy fraction points (Eq. 5) the stored energy can be retrieved from Eq. 2. The derivation of the stored energy, $J(t)$ with time or called here the stored efflux of energy $\dot{J}(t)$ between two energy fractions α_i and α_{i+1} gives the mean stored efflux of energy, $\dot{J}^{\alpha_i,\alpha_{i+1}}$ and can be determined as Eq. 19.

$$j^{\alpha_i,\alpha_{i+1}} = \frac{\Delta\alpha}{t_c(\alpha_{i+1}) - t_c(\alpha_i)}\Delta U \quad (19)$$

Similarly, the mean heat losses between the same two energy fractions α_i and α_{i+1} can be determined as Eq. 20. with $\dot{Q}_{loss}(\alpha)$ obtained from a combination of Eq. 12 and 14.

$$\dot{Q}_{loss}^{\alpha_i,\alpha_{i+1}} = \frac{\dot{Q}_{loss}(\alpha_i) + \dot{Q}_{loss}(\alpha_{i+1})}{2} \quad (20)$$

The mean total efflux of energy between two energy fractions is then the sum of the mean stored efflux of energy and the mean heat loss as in Eq. 21.

$$\dot{F}^{\alpha_i,\alpha_{i+1}} = j^{\alpha_i,\alpha_{i+1}} + \dot{Q}_{loss}^{\alpha_i,\alpha_{i+1}} \quad (21)$$

The prediction of the outlet temperature between two energy fractions can then be calculated from Eq. 22 with $T_{HTF,in}$ and $\dot{m}$ the inlet conditions and c_{HTF} the HTF specific heat capacity.

$$T_{HTF,out}{}^{\alpha_i,\alpha_{i+1}} = T_{HTF,in} - \frac{\dot{F}^{\alpha_i,\alpha_{i+1}}}{\dot{m}c_{HTF}} \quad (22)$$

3 Experimental set-up

Several designs of LTES systems have been proposed. The shell-and-tube design, with the PCM at the shell side and the HTF flowing through the pipes in the center, is considered most promising for devices for commercial heat exchangers, such as the double-pipe heat exchanger and shell-and-the tube heat exchanger, because of their high-efficiency in a minimum volume, simple design and large heat transfer area [58, 89-91]. The considered LTES system in this works is such a shell-and-tube LTES unit and has been designed for waste heat recovery at a temperature of around 250 °C and more specifically for interconnecting it with an organic Rankine cycle (ORC) [14]. The ORC connected to the LTES unit has a rated capacity of 11 kW_e and is designed for low heat source temperatures between 80 °C and 150 °C and uses R245fa as working fluid [92]. The storage capacity and the configuration of the LTES unit has been selected based on the working conditions of the ORC so a stable operation of the ORC solely on the stored heat can be realized for at least one hour [14]. A PCM shell-to-tube ratio of 5.25 has been used which is close to the optimal shell-to-tube ratio of 5.4 reported by Seddegh et al. [93, 94].

3.1 Set-up description

The storage system is composed of a rectangular enclosure with 36 steel tubes of 6 m length. To improve the heat transfer rate, each tube is outfitted with 545 radial hexagon shaped aluminium fins with a circumradius of 5 cm. The LTES unit is depicted in Figure 4 together with a cross-sectional schematic of the LTES unit. A comprehensive summary of the design parameters of the LTES system is given in Table 1.

Pure salts with high storage capacity, low cost and low environmental impact are developed as potential candidate for thermal energy storage of solar energy or industrial process heat [95]. Nitrates and their binary or ternary eutectic mixtures with desirable characteristics such as negligible supercooling, chemical stability are considered PCMs for the temperature range of 200-300 °C [95, 96].

Table 1. Overview of LTES design parameters

Item	Symbol	Value	Unit
	Storage		
Enclosure material	-	P265GH steel	-
Enclosure length	l_{ap}	7.43	m
Inner cross section	a_{ap} x b_{ap}	0.706 x 0.5	m
HTF type	-	Therminol 66	-
	Tube		
Material	-	16Mo3 steel	-
Number of tubes	n_t	36	-
Tube length (+ effective PCM length)	l_t	6 (5.46)	m
Inner diameter	DI	14.9	mm
Outer diameter	DO	21.3	mm
Fin apothem (regular hexagon)	a	4.3	cm
Fin circumradius	$R (=t)$	5.58	cm
Fin thickness	s_f	1	mm
Number of fins per tube	n_f	545	-
	PCM		
Material	-	Eutectic KNO_3-$NaNO_3$	-
Total PCM mass	m_{pcm}	3637	kg

With the intended application of waste heat recovery at a temperature of around 250 °C the storage material used is a binary eutectic mixture of KNO_3 and $NaNO_3$ with mass ratio 54-46% and a melting temperature of around 221 °C. The shell side has been filled with a total amount of 3637 kg. The properties of the PCM are retrieved from literature and presented in Table 2. Upper and lower limits for the thermal properties are given as conflicting values were found in literature [88, 95-99]. Orozco et al. [96] explains the difference in the values of the enthalpy of fusion and the heat capacities by the potential presence of impurities in the samples used for differential scanning calorimetry analysis.

Table 2. Thermal properties of the eutectic KNO_3-$NaNO_3$ PCM

	Symbol	Value	Unit
Melting temperature	T_{mlt}	221 - 226	°C
Solid specific heat capacity	$C_{p,s}$	1.350 - 1.420	kJ/kgK
Liquid specific heat capacity	$C_{p,l}$	1.460 - 1.673	kJ/kgK
Latent heat of fusion	Δh_p	92 - 106	kJ/kg
Solid density	ρ_s	2050	kg/m³
Liquid density	ρ_l	1960	kg/m³

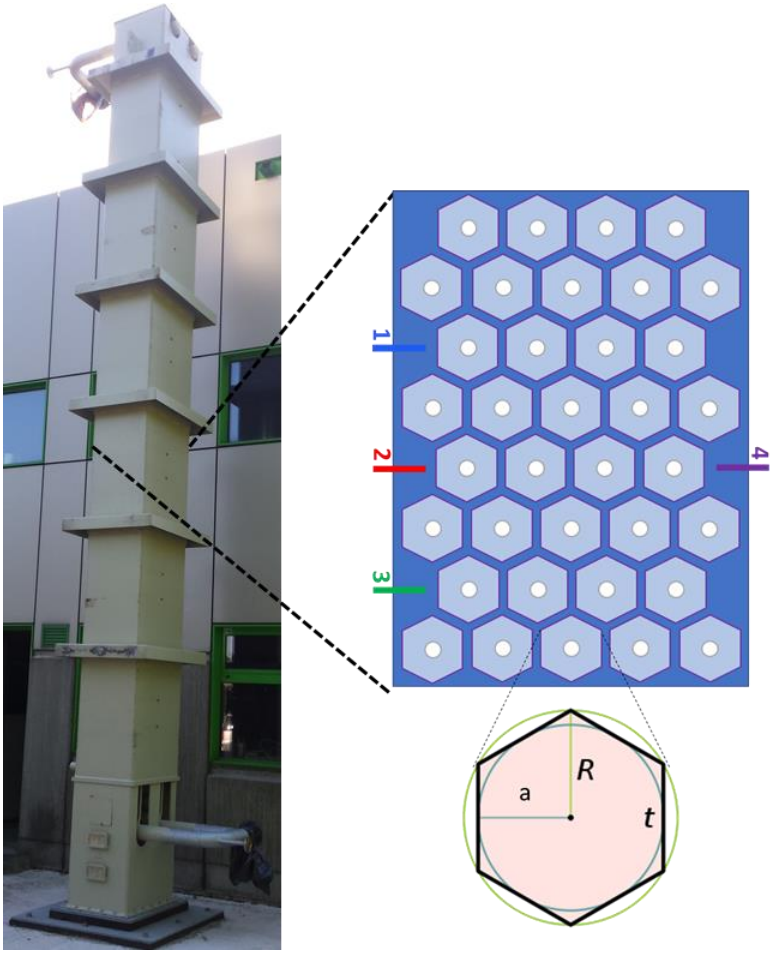

Figure 4. Cross sectional view of the shell-and-tube LTES battery. Dimensions of *a*, *R* and *t* are given in Table 1. At 26 different axial positions the PCM temperatures are measured at positions 1, 2, 3, 4.

The LTES unit is interconnected via a thermal oil circuit with a 250 kW electrical heater providing the energy required for charging. The thermal energy is supplied to the HTF (Therminol 66) by ten 25 kWe electrical resistances of which two elements can be set with a resolution of 1W. A constant speed pump and a position controlled three-way valve are used to set the desired mass flow rate of the HTF to the LTES unit. The flow direction of the HTF through the storage unit is set by a set of electronically actuated ball valves. For charging, the HTF flow is always from top to bottom to deal with PCM volume expansion while melting. For discharging the HTF flow is reversed. A brazed plate heat exchanger, connected to a water-glycol cooling circuit, is present in the oil circuit to serve as a load during the discharging phase of the battery. The water-glycol cooling circuit has a maximum operational temperature of 120 °C and has a maximum rated capacity of 480 kW_{th} in the temperature range 70 - 90 °C. For each experiment, the LTES unit is initialized to a uniform starting temperature by circulating the HTF through the tubes at the desired starting temperature. Before charging or discharging the LTES unit is first bypassed and the HTF is set to the desired testing temperature. When the HTF has reached the desired testing temperature the HTF flow is diverted to the LTES unit and the flowrate is set as quickly as possible to the desired test flow rate.

In the thermal oil circuit, the temperature is measured by Pt100 resistance thermometers class A with an accuracy of ±(0,15 + 0,002.T[°C]). The HTF temperature at the top and bottom of the storage system is directly measured at the HTF collectors of the storage unit. The HTF mass flow rate through the storage system is measured by a compact conditioning orifice plate flow meter of the type Rosemount 3051SFC. The mass flow rate can be measured in both directions and has an accuracy of 1 % when the mass flow rate is larger than 1.18 kg/s. All sensors and actuators of the thermal oil and water-glycol circuit are connected to a PLC with a sample frequency of 2 Hz. The temperatures of the PCM are analysed with K-type thermocouples over the length of the storage nearly every 20 cm at different locations as indicated in Figure 4 by the numbers 1 to 4. PCM temperatures are acquired every 10 seconds with a Keithley 2701 multiplexer. Mean values for each axial position are considered for further analysis. Visualization and control of the process is done by a LabView program version 16.0 on a desktop PC. The data is written to a .csv-file. Post processing of the measurements is done using Python version 3.8.

3.2 Experimental results

The energy balance for the four experiments is checked by estimating the total energy stored in the HTF, the metal parts of the container and the PCM between the initial state and the final state at the end of a charging process of the battery and comparing it with the integrated efflux of energy. The conservation of energy can be expressed for a control volume over the battery with a single inflow and outflow of HTF and heat losses to the environment as depicted in Figure 5.

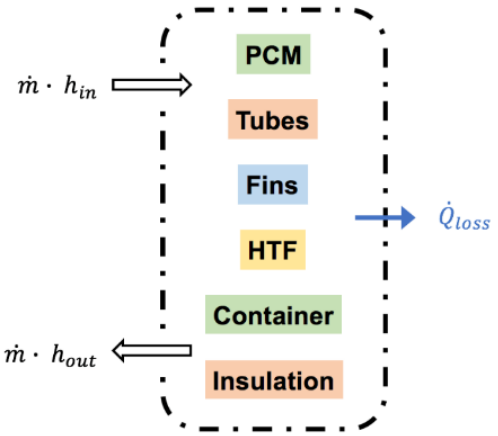

Figure 5. Control volume of the battery with single inflow and outflow of HTF and heat losses to the environment.

A charging cycle is started with a uniform temperature below the phase change temperature of the PCM and finished at quasi steady state with the battery temperature approaching the HTF inlet temperature which is above the PCM phase change temperature. The stored energy in each constituent at the end of the cycle t_{end} is given by Eq. 23.

$$\int_{t_{start}}^{t_{end}} U(T(t))\, dt = U(T_{end}) - U(T_{start}) = \Delta U(T_{start}, T_{end}) \qquad 23$$

The internal energy change of the battery is split in the internal energy change of the HTF U_{HTF}, the PCM U_{PCM}, the insulation U_{ins} and the metal U_{metal} which consist of the HTF tubes and the two collectors, the fins and the container walls, as these are the materials constituting the thermal battery. The heat losses are estimated from a discharging cycle without HTF flow rate. The change in stored energy can then only be attributed to the heat losses which are a function of the average temperature

of the battery. This average temperature is retrieved from the measured PCM temperatures at different axial locations near the outside tubes as indicated in Figure 4. The storage unit is divided in control volumes for each axial position and an average temperature is calculated based on the four temperature measurements in that control volume. The average battery temperature is then calculated through a volume weighted average for each control volume.

In total four experiments are performed with an average HTF inlet temperature of 250 °C and increasing HTF mass flow rates (1.87, 2.42, 2.90, 3.24 kg/s) and the respective total energy change of the battery is given in Table 3, along with the integrated efflux of energy, the estimated heat losses and the deviation in the energy balance. The deviation is calculated as Eq. 25. The state of charge is calculated as in Eq. 24 with ΔU_{max} a cycle in which the battery temperature is increased from the initial temperature to the HTF inlet temperature. The state of charge at the end of a charging cycle is between 93-94 % for all experiments.

$$\alpha(t_{end}) = \frac{\Delta U(T_{start}, T_{end})}{\Delta U_{max}} \quad 24$$

The total heat losses, Q_{loss}, decrease with higher mass flow rates since the total charging time decreases. The faster change in temperature of the battery and the corresponding increasing heat losses are thus nullified by a shorter period of time in which heat is lost to environment.

$$dev = 1 - \frac{\Delta U(T_{start}, T_{end}) + Q_{loss}}{F} \quad 25$$

Table 3. Energy balance for the four experiments

Experiment	$\Delta U(T_{start}, T_{end})$ [kWh]	F [kWh]	Q_{loss} [kWh]	Deviation [%]	$\alpha(t_{end})$
1	202.15	225.47	19.72	1.59	0.94
2	201.63	211.10	15.54	-2.88	0.93
3	200.74	206.22	13.83	-4.05	0.93
4	201.91	205.18	12.84	-4.67	0.93

4 Finite volume model

The CTEF method requires a large experimental dataset and as a full experimental characterization is time consuming a finite volume model of the storage unit is constructed to generate a numerical dataset to calibrate a CTEF model. Moreover, the finite volume model allows to validate the proposed CTEF heat loss model through extraction of the evolution of the energy fraction over time whereas experimental techniques would not allow to accurately estimate heat losses.

4.1 Model description

The numerical shell-and-tube LTES model is a finite volume method expressing the conservation of energy and mass in the constituents of the LTES heat exchanger by discretizing in control volumes and solving the conservation laws. This results in a discretized version of the local temperature $T(\vec{x}, t)$ in the control volumes while also the PCM control volume liquid fraction $\lambda(\vec{x}, t)$ is retrieved.

The model considers the HTF, the steel HTF tubes together with the aluminium fins and the PCM and is shown in Figure 6. The fins are considered indirectly by an increased effective thermal conductivity of the PCM, k_{eff} and hence are not depicted. The model considers convective heat transport in the HTF, transient forced convection heat transfer between the HTF and the tube wall, heat conduction in the axial direction of the tube wall, heat transfer between the tube wall and the PCM and axial and

radial heat conduction in the PCM. Heat transfer to the steel container, surrounding insulation and to the ambient are only considered indirectly by defining a constant loss factor UA_{loss}. The developed finite volume model is similar to a model developed by Barz et al. [100] and only serves as an efficient and fast tool to generate the dataset required to calibrate the CTEF model.

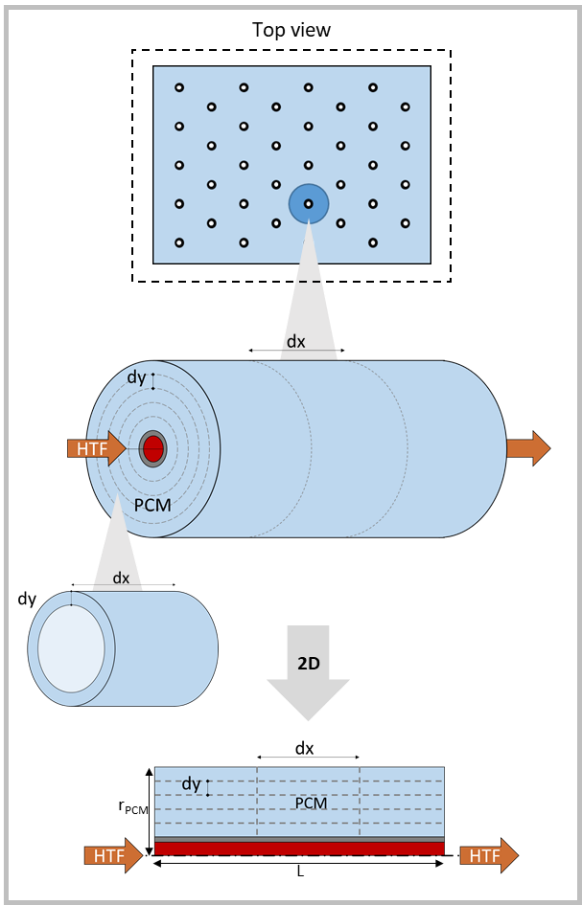

Figure 6. Computational domain of the finite volume model of a single tube representing the LTES unit.

For each tube of the LTES unit, an equal flowrate of the HTF and equal temperature on both the shell and tube side is assumed. As such only one tube is considered in the model as in Figure 6. Considering only one tube except of 36 tubes results in two modelling errors. First of all, the heat losses in the real LTES unit mostly affects the outer tubes while the present model averages the heat losses over all 36 tubes by considering all tubes identical. A second modelling error is the interaction between the melting fronts around the tubes. The first modelling error is thus assuming distributed losses while the losses are localized on the outer tubes [101]. However, the heat loss contribution to the energy balance is limited during the majority of the charging process. Therefore, the resulting error on the total efflux of energy is limited. The second modelling error could lead to an erroneous estimation of the local heat transfer rate as the melting fronts of different tubes interact. However, the overall heat transfer rate should be dominated by the regions in the storage where the PCM has not yet melted or the melting front has not progressed far. Furthermore, this error is reduced since the effective thermal conductivity is fitted to match the experiments to the finite volume predictions. Finally, the primary goal is not to investigate the details of the phase change process nor tracking the phase change progression. The main interest is to retrieve the outlet state of the HTF, the energy fraction and the heat losses over time with sufficient accuracy.

The forced convective flow of the HTF in the tube is modelled in 1D in the axial direction *x*. The HTF is modelled as an incompressible fluid with the thermal properties being temperature dependent. These properties are derived from the CoolProp library [102]. Furthermore, radial fluid flow, viscous dissipation, axial heat conduction in the fluid and external forces are neglected. The energy balance over the i^{th} HTF control volume as depicted in Figure 7 can be written as Eq. 26

$$m_{HTF}{}^{i} c^{i} \frac{dT_{HTF}{}^{i}}{dt} = [\dot{m}_{HTF} c T_{HTF}]^{i-1} - [\dot{m}_{HTF} c T_{HTF}]^{i} - \dot{q}_{HTF-wall}{}^{i} \quad 26$$

With $m_{HTF}$the mass of the HTF in the considered control volume, $\dot{m}_{HTF}$ the HTF mass flow rate, c the specific heat of the HTF and $\dot{q}_{HTF-wall}$ is the heat flux to the tube wall.

In Eq. 26 the mass of the considered control volume m_{HTF} is temperature independent because the density change of the HTF is neglected. The conservation of mass applied to any control volume with one inlet and one outlet results in an equal in- and outgoing mass flow rate, $\dot{m}_{HTF}$.

The heat flux $\dot{q}_{HTF-wall}$ to or from the tube wall is calculated from the heat transfer coefficient, h_c in the HTF tubes given in Eq. 27.

$$\dot{q}_{HTF-wall} = h_c A (T_{HTF} - T_{Tube}) \quad 27$$

The heat transfer coefficients are determined with Eq. 28 with the Nusselt correlations provided by the VDI Heat Atlas [103]. Constant heat flux boundary conditions are assumed with a hydrodynamically developed flow. Local Nusselt numbers at a point located at a distance *x* from the pipe inlet is calculated in each HTF control volume. For laminar flow, with Re ≤ 2300, the local Nusselt number is calculated from Eq. 29-31.

$$h_c = \frac{Nu k_{HTF}}{d_i} \quad 28$$

$$Nu_{x,q,1} = 4.354 \quad 29$$

$$Nu_{x,q,2} = 1.302 \sqrt[3]{Re \,\mathrm{Pr}\, d_i / x} \quad 30$$

$$Nu_{x,q} = \left\{ {Nu_{x,q,1}}^{3} + 1 + \left[Nu_{x,q,2} - 1 \right]^{3} \right\}^{1/3} \quad 31$$

Usually fully turbulent flow is considered at Re ≥ 10^4 but as outlined by Gnielinski a modified Petukhov-Kirillov correlation can be used in the turbulent region from Re ≥ 4000 given by Eq. 32-33 [104, 105] .

$$Nu_x = \frac{(\xi/8) Re\, Pr}{1 + 12.7 \sqrt{(\xi/8)} \,(Pr^{2/3} - 1)} \left[1 + \left(\frac{d_i}{x} \right)^{2/3} \right] \quad 32$$

$$\xi = (1.8 \log_{10}(Re) - 1.5)^{-2} \quad 33$$

For the transition region between laminar and turbulent flow a linear interpolation as in Eq. 34-35 is used as described by Gnielinski [104, 105].

$$Nu_x = (1-\gamma)Nu_{lam,2300} + \gamma\, Nu_{turb,4000} \quad (34)$$

$$\gamma = \frac{Re - 2300}{4000 - 2300} \quad (35)$$

$Nu_{lam,2300}$ is calculated from Eq. 29-31 at *Re* = 2300 and $Nu_{turb,4000}$ is calculated from Eq. 32-33 at *Re* = 4000.

For each iteration the heat transfer coefficient is calculated with the control volume bulk HTF temperature first and afterwards recalculated to account for the difference between the fluid bulk temperature and the tube wall temperature. This is done by first calculating the heat transfer from the HTF to the wall and retrieving the tube inner wall temperature. The HTF properties are then re-evaluated at the tube inner wall temperature from which a new heat transfer coefficient is calculated (Eq. 28-35).

The tube wall temperature T_{Tube} is modelled in the axial direction, *x,* only assuming a constant temperature in the radial direction. Heat conduction in the axial direction and heat transfer at the inner and outer tube wall are considered. For the tube wall the conservation of energy is applied to the i^{th} metal control volume depicted in Figure 7 as in Eq. 36. The control volume is in contact with the first PCM control volume as well as with the HTF as shown in Figure 7.

$$m_{Tube}c_{Tube}\frac{dT_{Tube}{}^{i}}{dt} = \dot{q}_{HTF-wall}{}^{i} + \frac{T_{Tube}{}^{i-1} - T_{Tube}{}^{i}}{R_{x,wall}} - \frac{T_{Tube}{}^{i} - T_{Tube}{}^{i+1}}{R_{x,wall}} - \frac{T_{Tube}{}^{i} - T_{PCM}{}^{i,0}}{R_{y,wallPCM}} \quad (36)$$

The thermal capacity of the fins is lumped into the thermal capacity of the tube wall as done by Barz et al. [100]. Accordingly, $m_{Tube}c_{Tube}$ in Eq. 36 is in fact calculated as in Eq. 37.

$$m_{Tube}c_{Tube} = m_{wall}c_{wall} + m_{fin}c_{fin} \quad (37)$$

$R_{x,wall}$ and $R_{y,wallPCM}$ are the thermal resistance between adjacent control volumes in the *x* and *y* direction, respectively.

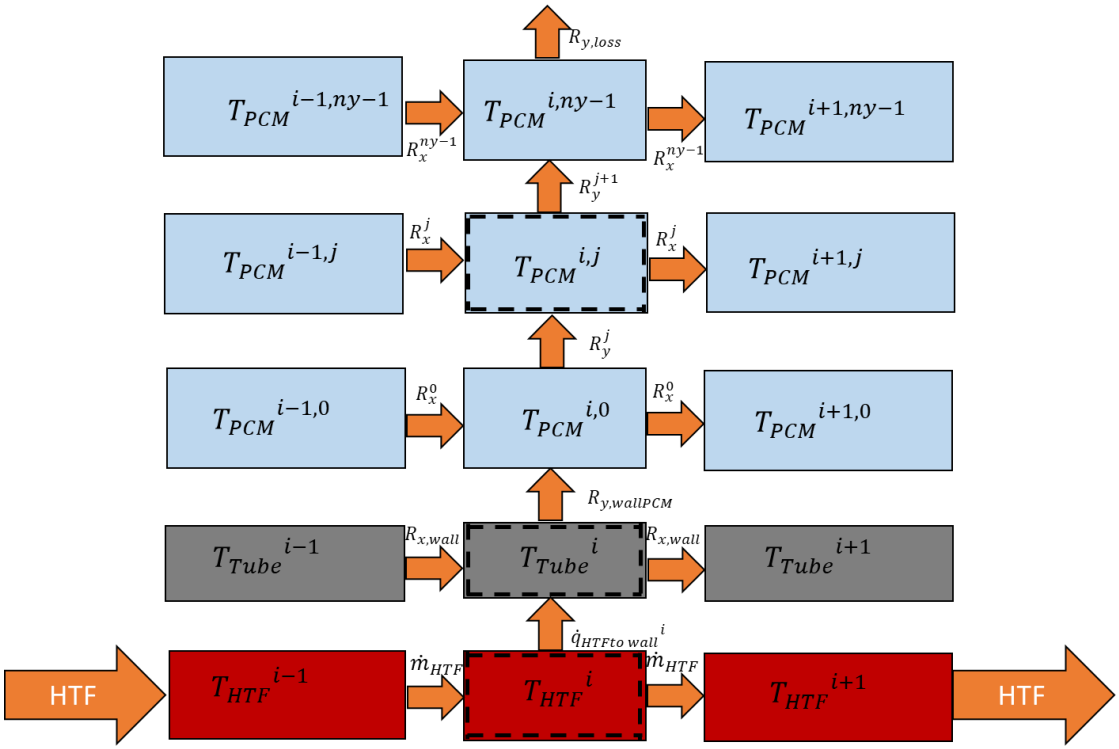

Figure 7. Schematic representation of the discretization scheme of the *i*-th control volume for the tube wall.

For modelling purposes the specific heat in the liquid region is considered temperature independent and 1.673 kJ/kg.K is used as proposed by D'Aguanno et al. [97], while for the specific heat in the solid region 1.35 kJ/kg.K is used as an average of the values found in the work of Tamme et al. [95] and Orozco et al. [96]. In the work of Vogel et al. [99] this value is also used. For the latent heat of fusion 100 kJ/kg is used as indicated in the work of Tamme et al. [95]. This value lies in between the value found by Orozco et al. [96] (92 kJ/kg) and given by Mohamed et al. [98] and Vogel et al. [99] (107 kJ/kg).

Heat transfer in the PCM shell is controlled by heat conduction in both the radial and axial direction. Natural convection in the liquid phase is ignored. Although it is often shown that natural convection can play a significant role during melting, the relative importance depends on the specific configuration of the storage unit or the PCM [54, 62, 106]. In the absence of extended heat transfer surfaces Tehrani et al. provides a guideline when it is safe to neglect natural convection based on a critical specific geometry [107]. However, the specific fin and tube configuration is used and is the same as described in the work of Vogel and Johnson [62]. Vogel and Johnson show that natural convection only has a minor impact due to the presence of the substantial amount of radial fins with a fin spacing less than 1 cm which inhibits natural convection.

Because of the introduction of aluminium fins the heat transfer is enhanced. This heat transfer enhancement is considered only indirectly by prescribing an improved thermal conductivity in the radial and axial direction of the PCM applying an effective thermal conductivity, k_{eff}. This approach is often applied to analyze the transient heat transfer problem for extended structures [73, 81, 87, 99] and porous structures such as metal foam [61, 108] but also for the heat transfer enhancement through the role of natural convection [48, 67, 87, 109, 110]. The accuracy of modelling a phase change process through an effective thermal conductivity depends on the application, but as the role of natural convection is limited in this case and the heat transfer process is thus conduction dominated

this is a sufficiently accurate simplification for this work. A similar approach has been used and validated through CFD by Vogel et al. for both branched longitudinal fins where natural convection can not be ignored and for the same radial fin structures as used in this work [99]. The effective thermal conductivity can be expressed as a combination of a parallel and serial arrangement with a parallelism factor describing the main direction of heat conduction through the composite fin/PCM arrangement [73]. However, this factor depends on the type of fin configuration and therefore requires fitting to experimental data [99]. Alternatively, the effective thermal conductivity can be fitted directly to experimental data as done in this work. Through this fitting process also any specific contribution and enhancement of the heat transfer process through natural convection will be considered indirectly.

The phase change is modelled using an apparent heat capacity ($\tilde{c}_p$) method [111]. A melting region between a lower limit $T_{mlt,l}$ and an upper limit $T_{mlt,u}$ is considered between 221-223°C. By using the apparent heat capacity method, an explicit treatment of the phase change front is avoided. Mixed material properties with a smooth transition between phases (solid, mushy, and liquid) are then applied over the entire region of the PCM [100]. Sigmoid functions [111-113] or smoothed heaviside functions [114] have been used in other works but the correlation for the apparent specific heat capacity $\tilde{c}_p(T_{PCM})$ (Eq. 38) used in this work is modelled using a combination of a piecewise linear term for the specific sensible heat $c_{p,P}(T_{PCM})$ (Eq. 39) and a normal probability distribution function (PDF) $\phi(T_{PCM})$ for the specific latent heat as done in the work of Barz et al. [100].

$$\tilde{c}_p(T_{PCM}) = c_{p,P}(T_{PCM}) + b(\phi(T_{PCM}) - c) \quad (38)$$

$$c_{p,P}(T_{PCM}) = a_0 + a_1 T_{PCM} \quad (39)$$

For the piecewise linear term (Eq. 39) when T_{PCM} is smaller than the lower melting temperature $T_{mlt,l}$, the heat capacity is assumed constant and equal to the solid heat capacity $c_{PCM,s}$. In a similar way, when T_{PCM} is larger than the upper melting temperature $T_{mlt,u}$, the heat capacity is assumed constant and equal to the liquid heat capacity $c_{PCM,l}$. By taking into account the offset, c and the multiplication factor, b the implemented correlation is shown in Figure 8. More information on the PDF parameters used is given in Appendix A.

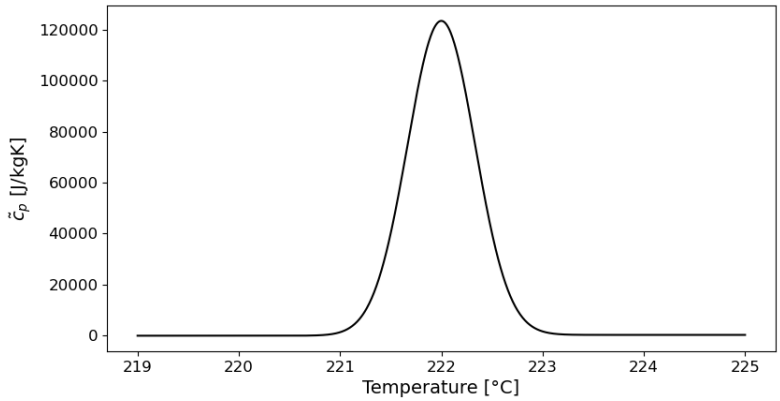

Figure 8. The implemented correlation of the apparent specific heat capacity $\tilde{c}_p(T_{PCM})$.

The energy balance for the PCM applied to the *i*th PCM control volume as depicted in Figure 7 is given in Eq. 40 and is expressed in terms of the PCM temperature T_{PCM} applying the apparent specific heat capacity, $\tilde{c}_{p,PCM}$. The PCM domain is divided in n_x control volumes in the flow direction and n_y control volumes in the radial direction.

$$m_{PCM}{}^{j}\tilde{c}_{p,PCM}{}^{j}\frac{dT_{PCM}{}^{i,j}}{dt}=\frac{T_{PCM}{}^{i-1,j}-T_{PCM}{}^{i,j}}{R_x{}^{j}}+\frac{T_{PCM}{}^{i+1,j}-T_{PCM}{}^{i,j}}{R_x{}^{j}}+\frac{T_{PCM}{}^{i,j-1}-T_{PCM}{}^{i,j}}{R_y{}^{j}}+\frac{T_{PCM}{}^{i,j+1}-T_{PCM}{}^{i,j}}{R_y{}^{j+1}} \quad (40)$$

With $m_{PCM}{}^{j}$ the mass of the considered control volume, R_x the thermal resistance between two adjacent PCM elements in the axial direction. This resistance depends on the radial position since the area of the annulus increases with increasing radius, which gives rise to an increased heat transfer surface area. R_y is the thermal resistance between two adjacent PCM elements in the radial direction. This resistance depends also on the radial position since the area of the shell of the PCM cylinder increases with increasing radius. For PCM control volumes located at the outer edge of the cylindrical shell domain, $R_y{}^{j+1}$ in Eq. 40 is replaced by a resistance to the surroundings, $R_{y,loss}$, as in Eq. 41. The surrounding air is assumed to be on temperature T_{amb}. This resistance, $R_{y,loss}$ is related to a heat transfer coefficient which represents the losses of the total storage system, UA_{loss}, and needs to be fitted from experimental data. As in the finite volume model only one tube is considered this global heat transfer coefficient is scaled with the number of tubes, N_{tubes} and the number of control volumes along the flow direction, n_x.

$$R_{y,loss}=\frac{1}{UA_{loss}}N_{tubes}n_x \quad (41)$$

The energy balance of the HTF, tube wall and PCM for each control volume are written in a sparse system of ordinary differential equations (ODEs) in the form presented in Eq. 42.

$$\frac{dT}{dt}=A.T+C \quad (42)$$

This set of ODEs is integrated in time using the Python Scipy package with a constant time step depending on the chosen number of timesteps, Nts [115]. The Jacobian of the set of equations is provided for faster and efficient solving of the set of ODEs.

Validation of the proposed CTEF heat loss model as in Eq. 11 requires knowledge of the energy fraction function, $\alpha(t)$, the efflux of energy, $\dot{F}$ and the heat losses, $\dot{Q}_{loss}$. The finite volume model allows to retrieve this information as function of time. Similarly to the experiments, the efflux of energy over the entire LTES unit is calculated as in Eq. 43.

$$\dot{F}=\dot{m}_{HTF}\left(h_{HTF,in}-h_{HTF,out}\right) \quad (43)$$

Heat losses of the entire LTES unit can be retrieved from the PCM temperatures at the edge of the PCM shell. For every timestep the mean PCM surface temperature is calculated over all control volumes located at the outer edge in the flow direction n_x. The calculation of the mean PCM surface temperature is substituted in Eq. 12 and then the heat loss at time *t* is expressed as Eq. 44 with UA_{loss} the overall heat transfer coefficient for the entire LTES unit.

$$\dot{Q}_{loss}(t)=\left[\frac{\sum_{x=0}^{x=n_x}T_{PCM,n_y-1}(t)}{n_x}-T_{amb}(t)\right].UA_{loss} \quad (44)$$

To obtain the stored energy of the LTES, $J(t)$ the efflux of energy and heat losses are integrated. The energy fraction, $\alpha(t)$ of the battery can then be retrieved from Eq. 48.

$$F(t) = \int_{t_{start}}^{t} \dot{m}_{HTF} \left(h_{HTF,in} - h_{HTF,out}\right) dt \quad 45$$

$$Q_{loss(t)} = \int_{t_{start}}^{t} \dot{Q}_{loss}(t) dt \quad 46$$

$$J(t) = F(t) - Q_{loss}(t) \quad 47$$

$$\alpha(t) = \frac{J(t)}{\Delta U} \quad 48$$

The model is discretized in two dimensions with n_x control volumes in the flow direction and n_y control volumes for the PCM in the cross section.

Grid convergence is checked by comparing different grids: $(n_x = 15\,, n_y = 5)$, $(n_x = 30\,, n_y = 10)$ and $(n_x = 60\,, n_y = 20)$, using the method of Roache [116]. All grids are found to give satisfactory results compared to the experimental results. For the HTF outlet temperature the errors between two consecutive grids were all below 0.2 °C, which was also the case for a variation of the timestep from 1 to 5 s. Similarly, the error on the liquid fraction between two consecutive grids has been checked and deviations were always lower than 0.0006. With respect to calculation time it is advised to choose the lowest value of each parameter. However, a small timestep is desired during the initial phase of the charging cycle and difference in calculation time for a given grid size with more timesteps is rather small. Therefore a grid size of $n_x = 15\,, n_y = 5$ and a timestep of 1 s is chosen for the simulations which results in a calculation time between 40-50 seconds for a 6h charging experiment. Further details of the grid convergence study is given in Appendix B.

4.2 Model calibration and validation

The finite volume model is developed under several simplifying assumptions and the factors determining the heat transfer (k_{eff} and UA_{loss}) are subject to experimental uncertainty. As a result of the assumptions made and uncertainty, the finite volume model requires fitting to match the experimental results. In both the finite volume model and the CTEF model the UA_{loss} is fitted. In the remainder of the paper UA_{loss} referring to the FV model will be denoted $UA_{loss,f}$ and the UA_{loss} referring to the CTEF model denoted with $UA_{loss,c}$. To fit the FV model to the experiments, an objective function Z (Eq. 51), quantifying the deviation between the model prediction and experiments is required. The deviation is quantified using the average integrated temperature difference, $I_{\Delta T}$, between the measured and modelled HTF outlet temperature (Eq. 49) together with the error on the integrated efflux of energy at the end of the experiment (Eq. 50). As the two errors are added to obtain a single scalar value, the summed absolute temperature difference is divided by the measured mean temperature difference between inlet and outlet of the HTF to yield a value which is in the same order of magnitude as the value of the error on the energy. In Eq. 49 Nts is the number of timesteps used in the simulations.

$$I_{\Delta T} = \frac{\sum_{i=1}^{Nts} \left| T_{out,sim}^{i} - T_{out,exp}^{i} \right|}{Nts(\overline{T_{in,exp} - T_{out,exp}})} \quad 49$$

$$I_{\Delta F} = \frac{\left| F_{end,sim} - F_{end,exp} \right|}{F_{end,exp}} \quad 50$$

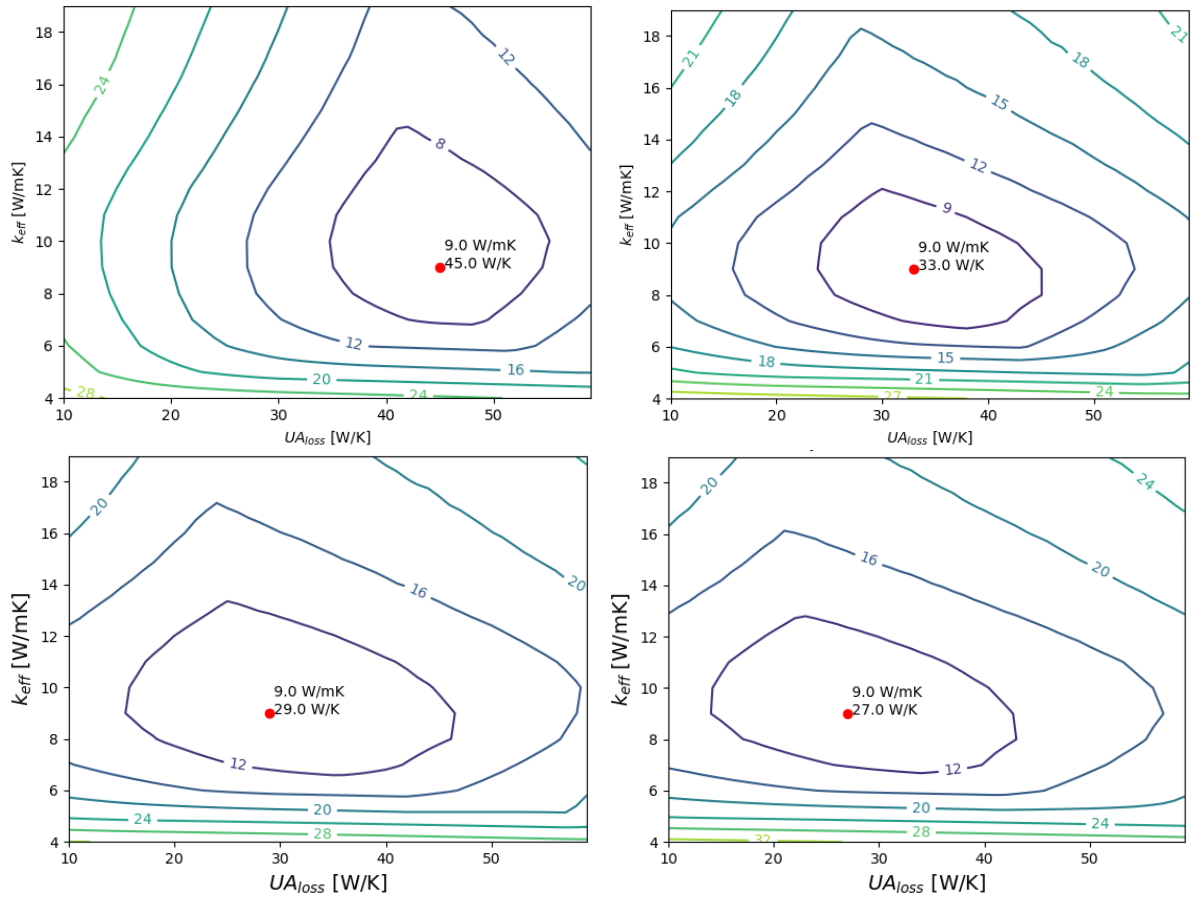

Figure 9. Residuals of the fitting process for the four different experiments. The optimal combination of k_{eff} and $UA_{loss,f}$ for each experiment is indicated in the corresponding graph.

The fitting strategy adjusts the conductive heat transfer resistance by directly altering the effective thermal conductivity, k_{eff} , of the PCM together with the overall heat transfer coefficient of the LTES unit, $UA_{loss,f}$, which determines the heat losses. The deviations between experiment and FV model prediction are calculated for all four experiments separately and the resulting contour plots showing the total error Z are shown in Figure 9. For each set the minimum total error in the grid is determined and shown on the contourplot. The optimal solution for the effective thermal conductivity for all experiments is the same (9 W/mK). The obtained effective thermal conductivity shows good agreement with the values presented in the work of Vogel et al. [99]. On the other hand the values found for the overall heat transfer coefficient decreases with increasing HTF mass flow rate.

The obtained fitting parameters are used to simulate the four performed experiments and compare the resulting HTF outlet temperature to the measured values. For each experiment the optimum values of k_{eff} and $UA_{loss,f}$ are used and the average absolute temperature difference and maximum absolute temperature difference are calculated. As the fitting for $UA_{loss,f}$ results in four different values the sensitivity of the model output is tested by also comparing the temperature differences using the average of the optimum $UA_{loss,f}$ values, $\overline{UA}_{loss,f}$ (= 33.5 W/mK) of the four experiments. The errors can be found in Table 4. The maximum error for all experiments occurs in the first 3 minutes where most of the transient phenomena occur. If this start-up phase is not considered the maximum error reduces to 0.92 , 1.46 , 2.27, 1.88 °C, for experiment 1-4 respectively. When $\overline{UA}_{loss,f}$ is used for the FV simulations, the mean and maximum errors remain nearly unchanged. After five minutes the maximum error further reduces to 1.54, 1.48, 2.29 and 2.09 °C, respectively. Since these errors are

close to the measurement error an alternative fitting strategy is not required and $\overline{UA}_{loss,f}$ will be used for further simulations.

Table 4. Mean and maximum temperature deviation with the optimum $UA_{loss,f}$ for each experiment and $\overline{UA}_{loss,f}$ over all experiments.

Experiment #	Mean error optimum $UA_{loss,f}$ [°C]	Max error optimum $UA_{loss,f}$ [°C]	Mean error with $\overline{UA}_{loss,f}$ [°C]	Max error with $\overline{UA}_{loss,f}$ [°C]
1	0.50	2.42	0.62	2.42
2	0.64	2.69	0.64	2.69
3	0.78	3.26	0.77	3.26
4	0.80	2.69	0.80	2.69

Figure 10 shows the measurement and the finite volume model prediction for experiment 1 with an target inlet HTF temperature of 250 °C and HTF mass flow rate of 1.87 kg/s. An $\overline{UA}_{loss,f}$ value of 33.5 W/K is used in the simulations. The yellow full line shows the predicted HTF outlet temperature while the green dashed line is the measured HTF outlet temperature. The red line is the measured inlet temperature and is also used as an input in the FV simulation.

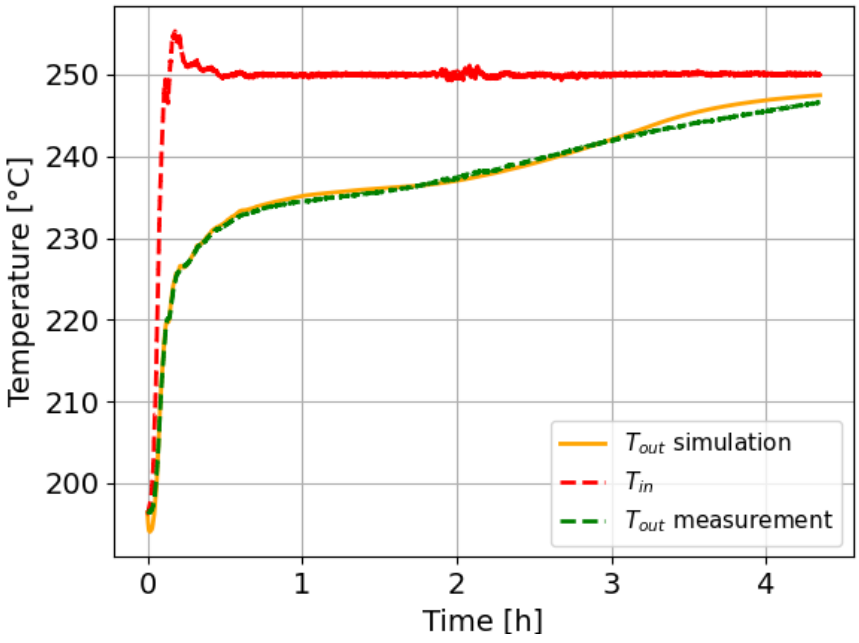

Figure 10. Comparison between simulated outlet temperature by the FV model and the measured inlet and outlet temperature

5 Charging time energy fraction model calibration

A total of 36 numerical experiments have been generated with the validated FV model with HTF mass flow rates between 1.8 and 3.3 kg/s and HTF inlet temperatures between 248 °C and 277 °C. For each experiment the initial battery temperature is set at 190 °C. The ambient temperature is set at 15 °C. The selection of appropriate inlet conditions for the characterization of the LHTES system is based on the CTEF method and the limitations of the actual set-up. The flow rates used are all in the turbulent flow regime. The different inlet conditions which form the experimental matrix are given in Table 5.

Table 5. CTEFM experimental matrix inlet conditions.

$T_{HTF,in}$ [°C]	248	251	255	260	267	277
$\dot{m}\ [\frac{kg}{s}]$	1.8	2.1	2.4	2.7	3.0	3.3

5.1 Fitting heat loss model parameters

The CTEF heat loss model as proposed in Eq. 16 requires fitting of UA_{loss} and power factor *n* as in Eq. 18. The corresponding residuals are minimal in the interval of $UA_{loss,c}$ [32-34.5] and are plotted in Figure 11A. In Figure 11B the combinations of $UA_{loss,c}$ and power factor *n* which minimize the residuals are plotted for $UA_{loss,c}$ values between 32.6 and 34.2 W/K. If $UA_{loss,c}$ increases, the power factor *n* should increase as well to minimize the residuals and multiple combinations of UA_{loss}-*n* can be used to minimize the objective function as the absolute value of these residuals fluctuate between 0 and 7 W and no trends could be observed. The actual lowest residual obtained corresponds with an $UA_{loss,c}$ value of 33.23 W/K and a power factor *n* of 1.885. As this $UA_{loss,c}$ value is close to the previously obtained average value of 33.5 W/K from the FV model fitting this combination is used in further analysis.

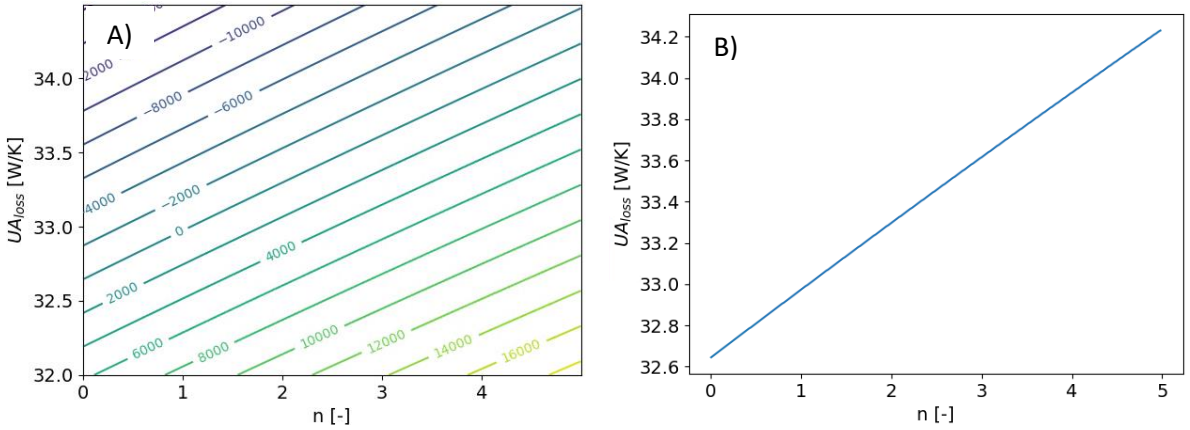

Figure 11. Fitting results for $UA_{loss,c}$ and *n* (Eq. 18). A) Contourplot of the residuals as function of $UA_{loss,c}$ and *n*. B) Combinations of $UA_{loss,c}$ and *n* which minimize the residuals.

Solving the heat loss model defined by Eq. 16 gives the energy fraction $\alpha(t)$ as function of time. The sensitivity of the model output for the energy fraction obtained at the end of the experiments, $\alpha(t_{end})$ to the fitted power factor *n* is tested. This is done by calculating $\alpha(t_{end})$ for each power factor, *n* in the interval 0-5 with a fixed $UA_{loss,c}$ value and comparing it with the values obtained from the FV model. This is done for the optimal $UA_{loss,c}$ value and also with the left bound and right bound limit of $UA_{loss,c}$ with the lowest residual values, 33.23, 32.6 and 34.2 W/K respectively. In all cases a deviation below 1% is observed and any $UA_{loss,c}$-*n* combination as given in Figure 11B gives satisfactory results. As this is a relative low error the proposed heat loss model and fitting strategy can be used to calibrate the CTEF model.

5.2 Charging time correlation fitting

Eventually Eq. 7 is fitted to the experiments for energy fractions ranging from $\frac{\alpha_{max}}{100}$ to α_{max}, with α_{max} the minimum energy fraction obtained at the end, $\alpha(t_{end})$, over all experiments. These outer limits are chosen because, namely 0 and $\alpha > \alpha_{max}$, do not have any predictive value since the charging time for a fraction of 0 is obviously 0 and the charging time for a fraction larger than α_{max} has no physical value for some experiments since these energy fractions are never reached due to the heat

losses. The fitting is performed in two steps. In a first step, the slope and intercept of Eq. 6 are determined for the six mass flow rate levels. In the second step, these slope and intercept values are fitted by the slope and intercept function as they appear in Eq. 7. The fitting coefficients as a function of the energy fraction are shown on Figure 12. The error bars represent the standard deviation of the fitted coefficients and are obtained from the variance of the coefficient estimate. This standard deviation for *A, B, C, D*, increases with the energy fraction from 0 to 3127, 0 to 7479, 0 to 45 and 0 to 107, respectively.

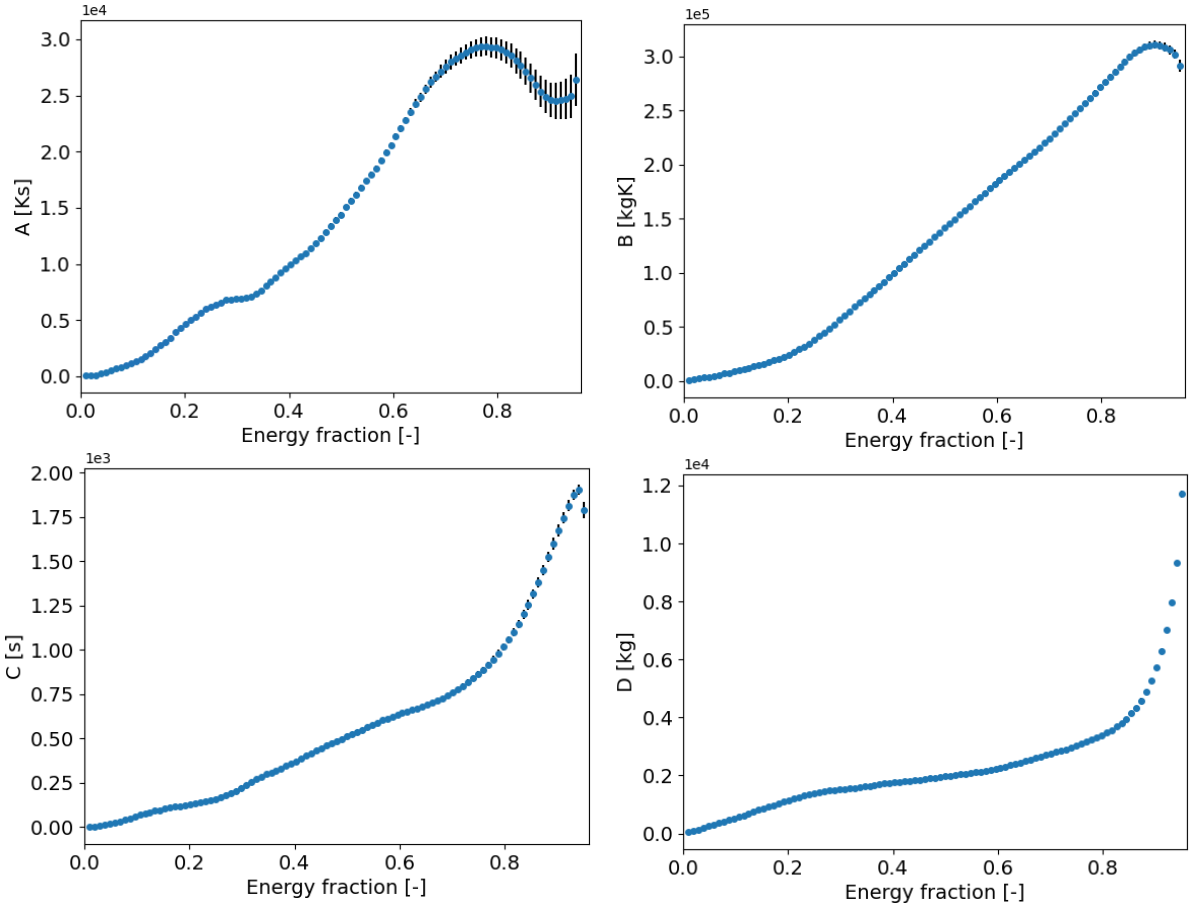

Figure 12. Fitting coefficients for the charging time correlation proposed in Eq. 7 as a function of the energy fraction.

6 Charging time energy fraction model evaluation

Figure 13 shows a flow chart of how to use the CTEF model to predict the HTF outlet temperature for given inlet and initial conditions. The selected inlet conditions and initial state of the experiment are combined with the calibrated charging time correlation and correlation parameters to determine the charging time for all energy fractions in the charging time set (Eq. 5). The maximum possible stored energy change is determined from the mass and properties of the constituent materials and the initial and final conditions (Eq. 4). The maximum possible stored energy change is combined with the charging time to estimate the stored energy (Eq. 2) which is differentiated to determine the stored efflux of energy. The heat losses are estimated from the heat loss model (Eq. 12+14). The stored efflux of energy and heat losses are added to give the total efflux of energy. Finally the outlet temperature is determined from Eq. 22.

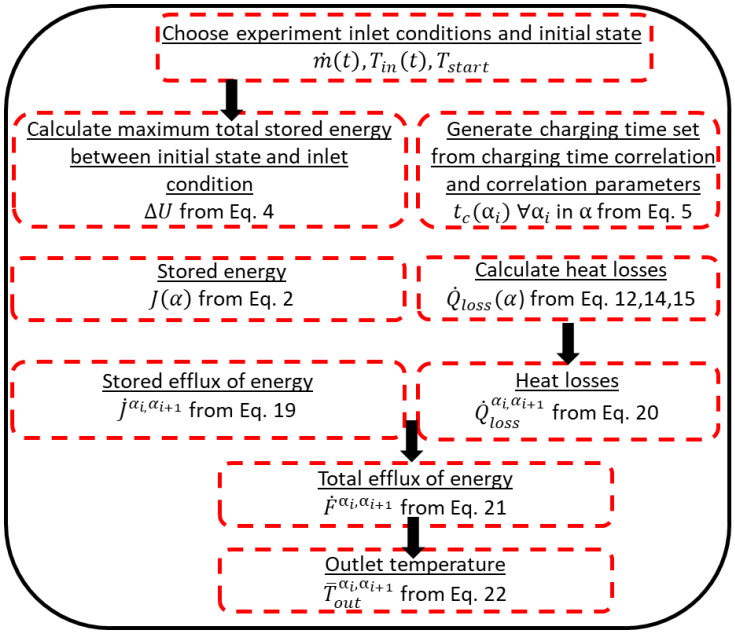

Figure 13. Flowchart representation of predicting the outlet temperature for known inlet and initial conditions with a fitted CTEF model.

6.1 Validation to calibration experiments

Firstly, the stored energy prediction from the CTEF heat loss model should be compared to the stored energy obtained from the FV model for all 36 experiments. Large deviations in the stored energy prediction will eventually result in incorrect calibration of the charging time correlation and lead to errors in the outlet state prediction. The criterion used to rate and compare is the integrated absolute difference between the CTEFM prediction and the FV model output as Eq. 52. This integrated absolute difference is in fact the average absolute difference as the timestep is constant and hence the number of timesteps used in the simulation (Nts) in the equation.

$$\frac{\sum_{t=0}^{t_{end}} \left| J_{LHTES,CTEF}(t) - J_{LHTES,FV}(t) \right|}{Nts} \qquad 52$$

The average integrated absolute difference between the CTEFM heat loss model prediction of the stored energy, $J_{LHTES,CTEF}$ and the FV simulations, $J_{LHTES,FV}$ across all 36 experiments is 0.68 kWh with a minimum and maximum of 0.76 and 1.43 kWh absolute difference at the end of the experiments. The experiment with the worst and best stored energy prediction happens to be the slowest and fastest charging experiment, respectively. The evolution of the stored energy for both experiments is shown on Figure 14. The black dashed lines indicates the maximum possible stored energy change between the initial starting condition and the HTF inlet temperature. The low errors proof that the proposed CTEF heat loss model and the described fitting methodology are accurate and suitable to predict the energy fraction as function of time which is necessary to calibrate the charging time correlation.

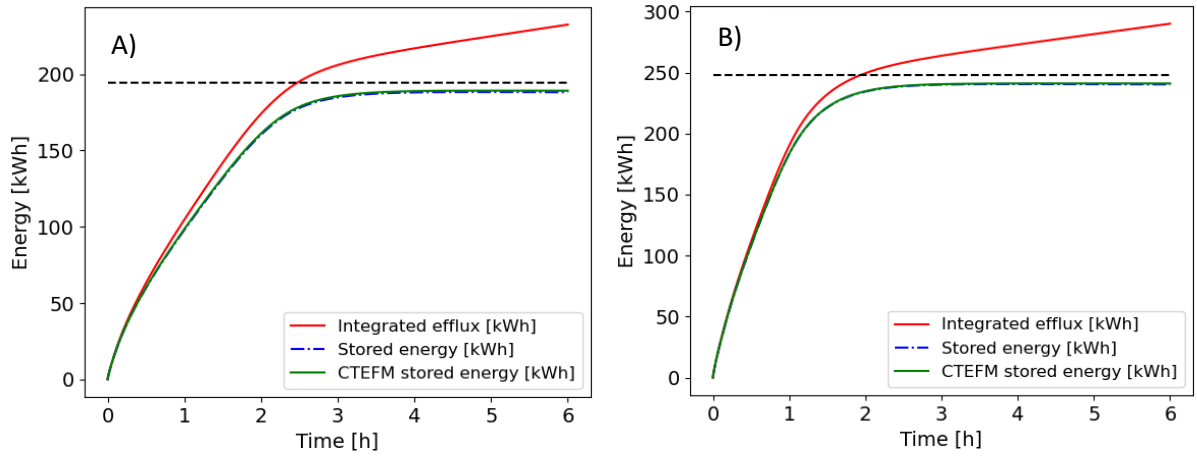

Figure 14. Comparison between the stored energy obtained from CTEFM heat loss model prediction with the FV simulation. A) for experiment with lowest mass flow rate and inlet temperature. B) For experiment with highest mass flow rate and inlet temperature.

Secondly, the deviation of the charging time given by the correlation (Eq. 7), $t_{c,cor}$ with the charging time obtained from the finite volume model as a function of the energy fraction is checked. This is calculated as in Eq. 53 and is plotted in Figure 15.

$$I_{t_c}(\alpha_j) = \frac{\left|t_{c,sim}(\alpha_j) - t_{c,cor}(\alpha_j)\right|}{t_{c,cor}(\alpha_j)} \qquad 53$$

The correlation achieves root mean square deviations well below 1% over all energy fractions with a maximum deviation of 3.1%.

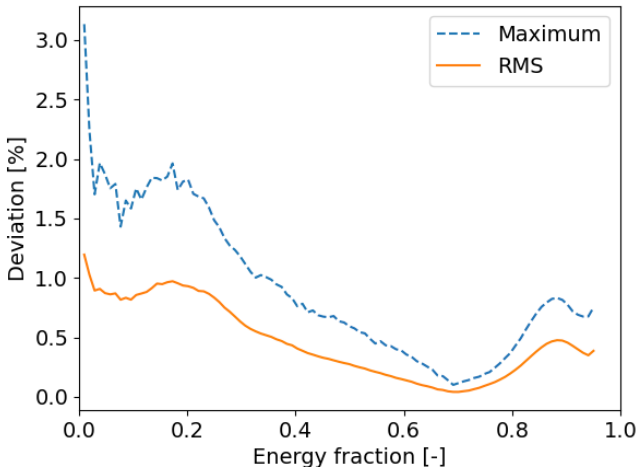

Figure 15. Root mean square and maximum deviation of the charging time correlation as function of the energy fraction.

Since both the CTEF heat loss model and charging time correlation are shown to accurately predict respectively, the energy fraction and the charging time, the workflow presented in Figure 13 can be used to predict the efflux of energy and the HF outlet temperature as a function of time. The predictive model is constructed by estimating the charging time for each energy fraction between 0 and 0.96 with a step of 0.0096. The resulting predictions can be compared to the measured outlet temperature, efflux of energy and energy as a function of time. The criterion used to rate and compare the fitting of the estimates to the measurements is based on the outlet temperature as this is a direct measurement and efflux of energy and stored energy are integrated values of this direct measurement. The absolute temperature difference between the measured and predicted outlet

temperature is integrated over time. This integrated value is then divided by the measured charging time $t_c(0.95)$ to retrieve the integrated absolute temperature difference $I_{\Delta T}(\alpha_j)$ as Eq. 54.

$$I_{\Delta T}(\alpha_j) = \sum_{i=0}^{j} \left(\left| \bar{T}_{out,}^{\alpha_{i+1}\alpha_i} - \frac{T_{out}(t_c(\alpha_{i+1})) + T_{out}(t_c(\alpha_i))}{2} \right| \frac{t_c(\alpha_{i+1}) - t_c(\alpha_i)}{t_c(0.95)} \right) \quad 54$$

The CTEFM is not successful for the early stages of charging [17]. Therefore the experiments are compared from a base energy fraction of 0.1 to a final energy fraction of 0.95. The experiment with the best fit is selected and the results of the stored energy, efflux of energy and temperature are shown in Figure 16A, B and C, while for the worst fit this is shown on Figure 17 A, B and C. For the best experiment the average absolute temperature difference is 0.28 °C between energy fractions 0.01 and 0.96 with a maximum deviation of 1.14 °C at energy fraction 0.01 which reduces to 0.52 °C at a later stage with energy fraction 0.2. Similarly, for the worst prediction the average absolute temperature difference is 0.50 °C with a maximum deviation of 2.58 °C at energy fraction 0.01 which reduces to 1.76 °C at a later stage with energy fraction 0.2.

The numerical experiments are plotted to reach an energy fraction of 0.96 while for the prediction of the correlation this is plotted for an energy fraction between 0.0144 and 0.9552. This is due to differentiating the correlated energy with respect to time to retrieve the efflux of energy from the change in energy fraction (Eq. 19).

Both the HTF outlet temperature and the efflux of energy are predicted reasonably well with the deviation being lower than the measurement accuracy. Also the deviation in the total integrated efflux of energy is small. For the best fit there is a deviation of the correlation to the simulation of 2.17 kWh or 1.05 % where the prediction overestimates the total integrated efflux. For the worst fit this increases to 3.21 kWh or 1.2 %. The error on the integrated efflux of energy is in absolute values the result of the correlation and is only partially attributed to the CTEF heat loss model. For the best experiment the deviation on the stored energy is 2.99 kWh and on the energy losses 0.82 kWh. As the predicted efflux of energy as heat loss is in the first 1.6 hours of the charging process consistently lower with a maximum deviation of 0.84 kW. After 1.6 hours the predicted heat loss is on average 0.03 kW too low. This is shown on Figure 18. As a result the energy lost at the end of the experiment is underestimated with 0.82 kWh for the best experiment.

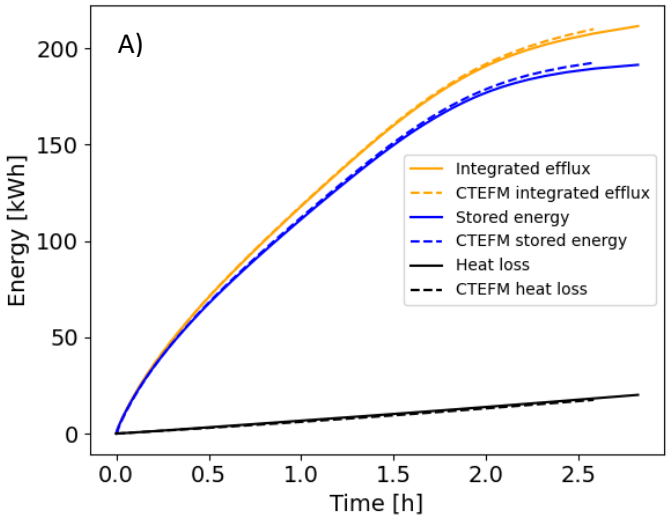

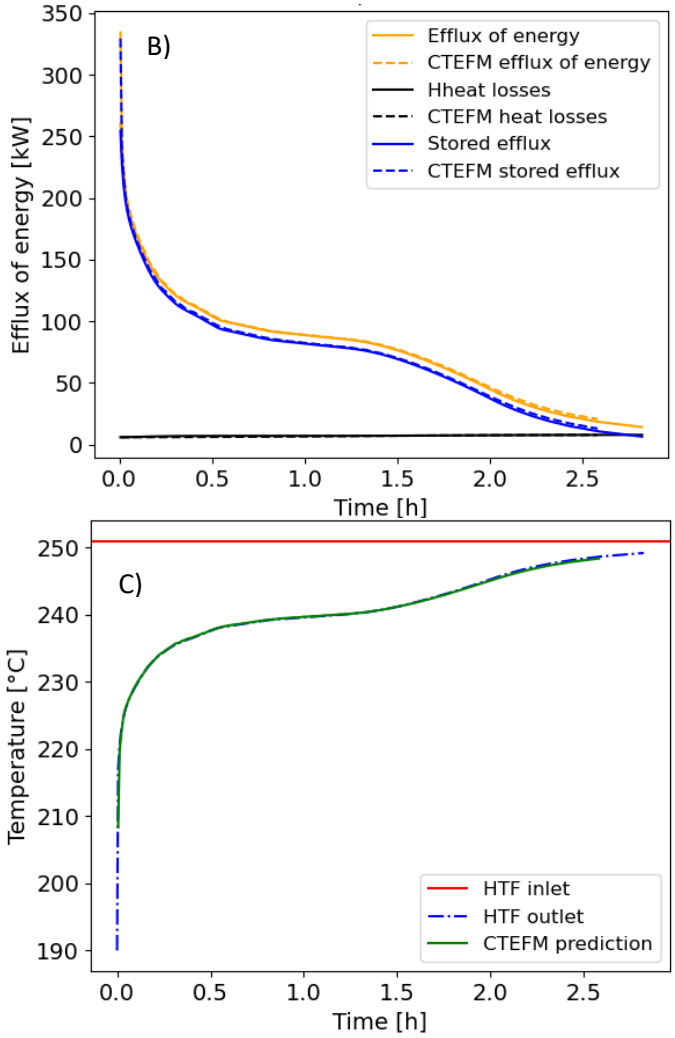

Figure 16. Comparison of predicted integrated efflux of energy (A), efflux of energy (B) and HTF outlet temperature (C) compared with the simulation data for the best prediction.

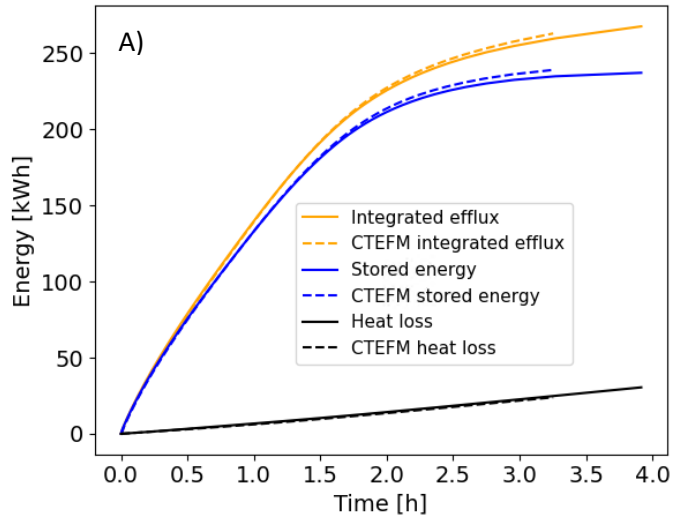

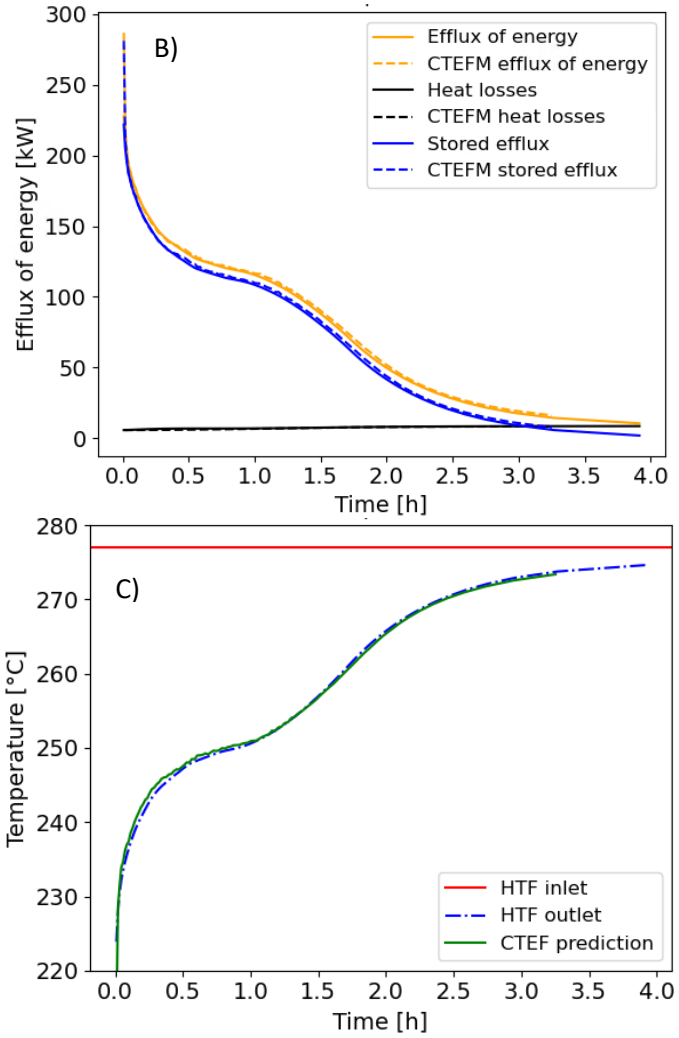

Figure 17. Comparison of the predicted integrated efflux of energy (A), efflux of energy (B) and HTF outlet temperature (A) with the simulation data for the worst prediction

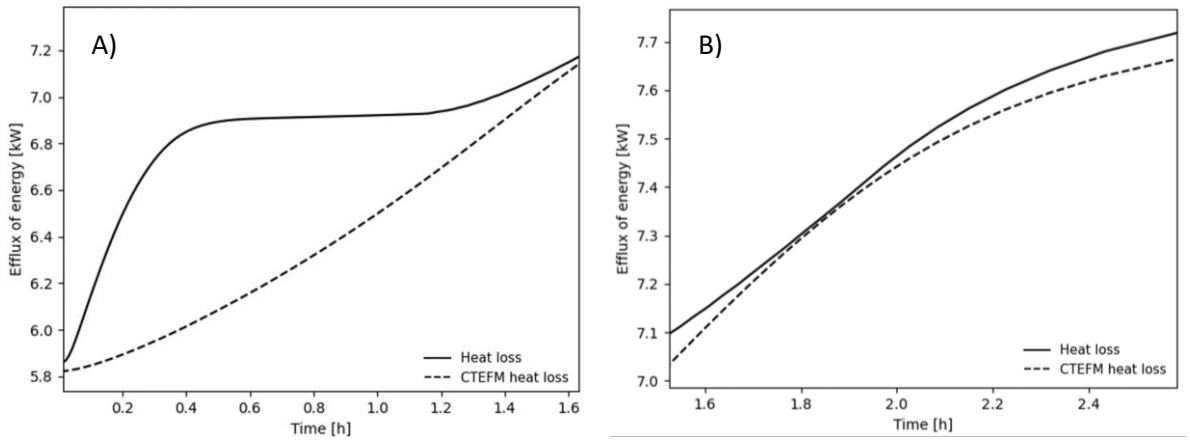

Figure 18. Comparison of the predicted heat losses with the simulated heat losses for the best experiment in the first 1.6 hours (A) and after the first 1.6 hours (B).

Figure 19A shows the integrated absolute temperature difference between the energy fraction 0.1 and 0.95 (A) and between 0.1 and 0.7 in Figure 19B for all performed experiments. The integrated difference varies between 0.44 °C and 0.07 °C with an obvious trend in the error as a function of the mass flow rate. Lower mass flow rates increase the total charging time significantly and the error on the correlation increases for higher energy fractions. The trend in the integrated difference as function

of $1/\Delta T$ is twofold. On the one hand, the error decreases with increasing $1/\Delta T$ and thus decreasing inlet temperature. This is because with lower inlet temperatures the temperature difference between in- and outlet decreases and as a result the error decreases. However this is only valid up to the inlet temperature of 251°C. After that, and thus for the lowest inlet temperature of 248 °C this error increases again. This trend remains unchanged when lower energy fractions are excluded. However, when the larger energy fractions are excluded this trend vanishes which can be seen from Figure 19. This is because for the lowest temperature differences it takes proportionally very long to obtain high energy fractions and the error on the correlation increases as the standard deviation on the fitting parameters *A, B, C* and *D* increase significantly with higher energy fractions.

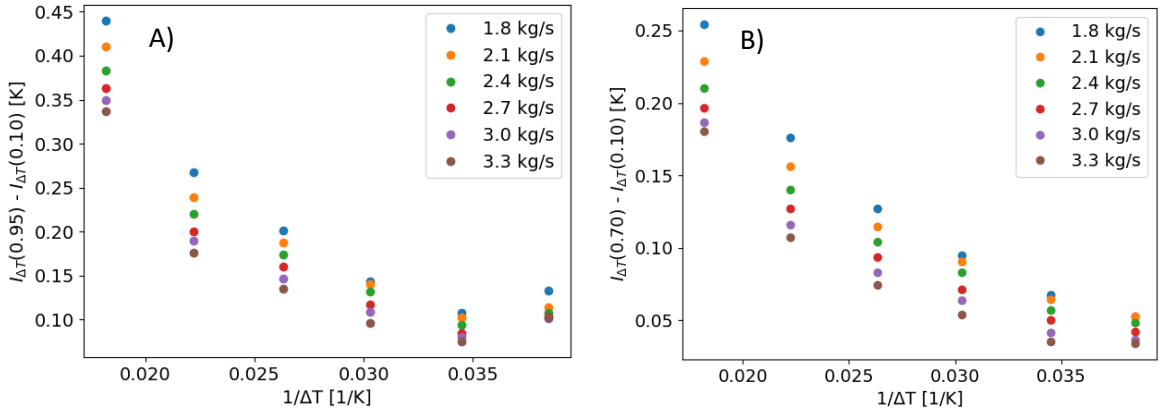

Figure 19. Integrated absolute temperature difference between the energy fraction 0.1 and 0.95 (A) and 0.1 and 0.7 (B) for all performed experiments.

6.2 Validation to real experiments

In the previous section the CTEF model has been validated on a dataset used to calibrate the model. Here, instead the predictive value of the CTEF model is presented for four numerically obtained experiments with a different mass flow rates and inlet temperatures than those shown in the experimental matrix (Table 5). The inlet and starting conditions for the numerical experiments are taken similar to the actual performed experiments. The initial PCM temperate is kept constant at 190°C and the HTF inlet temperature is constant at 250 °C. Only the mass flow rate is varied: 1.87 – 2.42 – 2.90 – 3.24 kg/s. An overview of the deviation between the predictions and the four numerical experiments is given in Table 6 while the predicted outlet temperature is shown on Figure 20.

Table 6. Average, maximum and integrated absolute temperature difference between CTEF model prediction and four numerical validation experiments.

$\dot{m}$ [kg/s]	Absolute average T deviation [°C]	Maximum T deviation [°C]	$I_{\Delta T}(0.95) - I_{\Delta T}(0.1)$ [°C]
1.87	0.1317	0.542	0.12
2.42	0.1126	0.606	0.11
2.90	0.0975	0.709	0.10
3.24	0.0885	0.676	0.09

The errors made by the CTEF model are low and the calibrated CTEF model accurately predicts the HTF outlet temperature when compared to the output of a numerical experiment which has not been used in the set for calibrating the CTEF model. The average calculation time to retrieve the HTF outlet temperature from the CTEFM correlation for an experiment is on average lower than 3 ms. This

includes the determining the heat losses with the heat loss model based on the fitted parameters UA_{loss} and factor *n* and calculating the charging time with the known fitting parameters *A, B, C, D.*

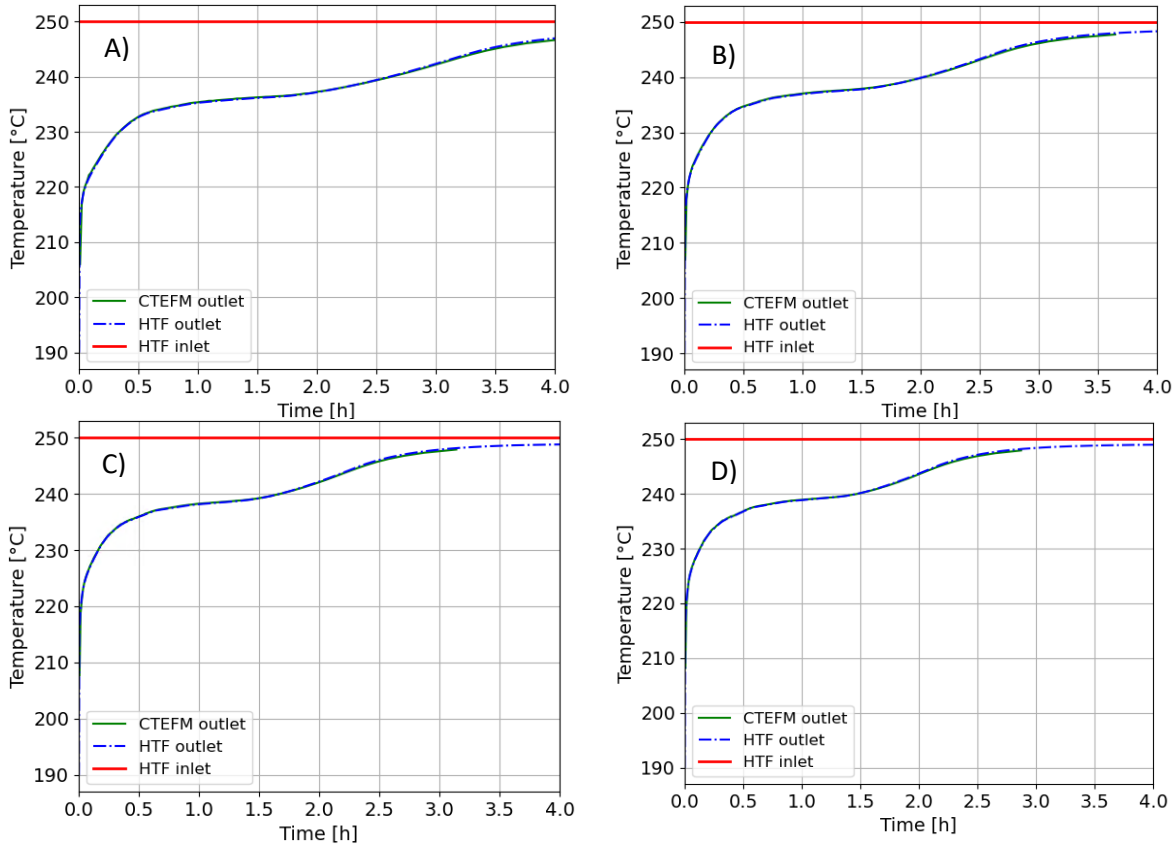

Figure 20. Comparison of the predicted outlet temperature by the CTEF model with the FV simulations for the four validation experiments with mass flow rate [kg/s]: A) 1,87 B) 2,42 C) 2,9 D) 3,24

The output of the CTEF model is also compared to the four actual performed experiments. The resulting deviations between energy fractions 0.95 and 0.1 are given in Table 7 while the predicted outlet temperature is shown on Figure 21. The input conditions for the CTEF model are kept constant while the actual input conditions are transient in nature and it takes a while to reach the target inlet temperature. As such the initial phase of the process is not well represented but overall the CTEF model predictions are close to the measurement accuracy. Experiments where the initial transient phenomena are minimal and the target inlet temperature is obtained fast are better predicted than those experiments where it takes a longer time to reach stable inlet conditions. Also note that the CTEF model has been calibrated on numerical experiments and there is already an error present between the FV simulations and real experiments (see Figure 10). Therefore it makes sense that the CTEF model predictions deviate from the real experiments.

Table 7. Deviation of the predicted outlet temperature with the measured outlet temperature for the four experiments.

$\dot{m}$ [kg/s]	Absolute average T deviation [°C]	Maximum T deviation [°C]	$I_{\Delta T}(0.95) - I_{\Delta T}(0.1)$ [°C]
1.87	0.81	1.94	0.65
2.42	0.95	4.71	0.76
2.90	1.22	12.18	1.00
3.24	1.83	14.35	1.38

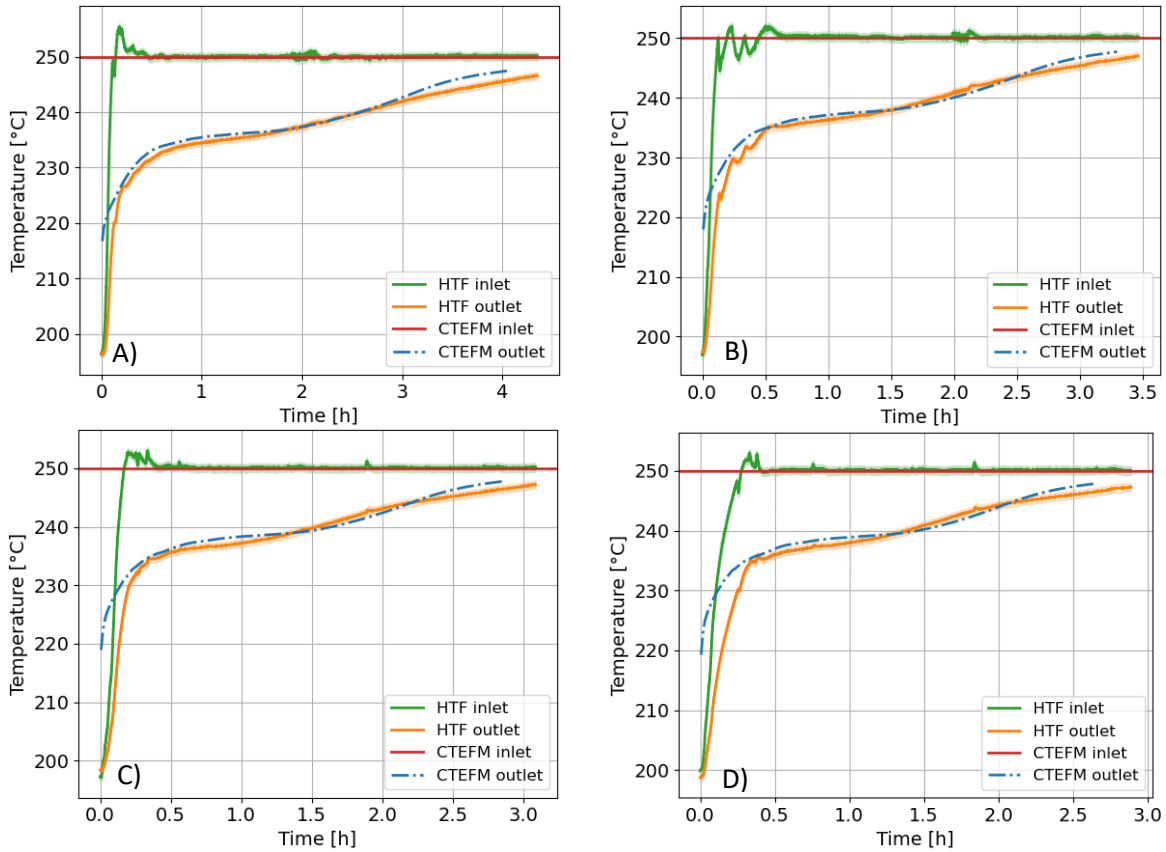

Figure 21. Comparison of the predicted outlet temperature with the measured outlet temperature for the four validation experiments with mass flow rate [kg/s]: A) 1,87 B) 2,42 C) 2,9 D) 3,24

7 Conclusion

In this paper the charging time energy fraction method is used to characterize a latent thermal storage unit. The charging time energy fraction method is firstly further developed and extended with a heat loss model. This heat loss model allows to use the charging time energy fraction method for LTES heat exchangers with considerable heat losses.

The major results of the study are listed below:

- A limited dataset of four experiments has been obtained from a shell and tube latent thermal energy storage system with a storage capacity of 220 kWhth between 190 and 250 °C.
- A finite volume model is calibrated on the unique dataset and fitting of the effective thermal conductivity of the fin/PCM material leads to a value of 9 W/mK for this specific tube-fin configuration while the obtained overall heat loss coefficient is 33.5 W/K.
- In this work the heat losses are on average between 5 to 8 kW at temperatures between 190 and 270 °C.
- A new heat loss model is added to the charging time energy fraction method and calibrated on an extensive numerical dataset
- The predicted energy fraction at the end of a charging process deviates on average less than 1% from the numerical data and therefore the heat loss model is validated.
- The charging time correlation is calibrated on 36 numerical experiments and achieves root mean square deviations well below 1% over all energy fractions with a maximum deviation of 3.1%.

- The improved charging time energy fraction model is validated on the unique experimental dataset and the average absolution temperature deviation between the predicted outlet temperature and the measured outlet temperature is 0.11 °C across the four tests.
- The initial start-up phase of the charging process is not well represented where the HTF inlet temperature is lower than the PCM melting temperature but still higher than the battery temperature. This is on the one hand because start-up phenomena were not included in the finite volume model simulations on which the charging time energy fraction model has been calibrated and on the other hand a constant input condition is required for the model which deviates from the actual inlet condition.

The charging time energy fraction method has thus been demonstrated to be able to characterize storage systems for industrial purposes with significant heat losses and is now proven to work for different LTES configurations. However, as transient inlet conditions are not uncommon in industrial processes the charging time energy fraction method should be further investigated to able to handle these conditions. Besides, the influence of changing geometrical properties and PCM thermal properties on the fitting parameters *A, B, C, D* is not completely known. As such the charging time energy fraction method is not a design method. Further additional parametric analysis can be performed to fully elucidate the underlying functions behind the fitting parameters *A, B, C* and *D*.

Acknowledgements

This research was within the frame of the VLAIO-CORNET project HBC.2016.0330 "Short term heat and cold storage in industry - Shortstore", funded by the Institute for the Promotion and Innovation by Science and Technology in Flanders. This study has received funding from European Union's Horizon 2020 research and innovation programme under grant agreement Nº 657466 (INPATH-TES).

References

1. European Commission. *European green deal*. 2019 [cited 2022 January 31]; Available from: https://ec.europa.eu/info/strategy/priorities-2019-2024/european-green-deal_en
2. Commission, E., *Directorate-General for Climate Action, Going climate-neutral by 2050 : a strategic long-term vision for a prosperous, modern, competitive and climate-neutral EU economy.* Publications Office, 2019.
3. European Commission. *Why the EU supports energy storage research and innovation*. 2020 [cited 2022 March 21]; Available from: https://ec.europa.eu/info/research-and-innovation/research-area/energy-research-and-innovation/energy-storage-and-distribution_en.
4. European Commission, *A EU Hydrogen Strategy*. 2020.
5. European Association for Storage of Energy, *Energy Storage for a Decaronised Europe by 2050.* 2019: Brussels.
6. European Association for Storage of Energy, *Thermal Storage Position Paper*. 2017: Brussels.
7. European Commission. *Horizon Europe*. [cited 2022; Available from: https://ec.europa.eu/info/research-and-innovation/funding/funding-opportunities/funding-programmes-and-open-calls_en.
8. Lacroix, M., *Numerical-Simulation of a Shell-and-Tube Latent-Heat Thermal-Energy Storage Unit.* Solar Energy, 1993. **50**(4): p. 357-367.
9. Lacroix, M., *Study of the Heat-Transfer Behavior of a Latent-Heat Thermal-Energy Storage Unit with a Finned Tube.* International Journal of Heat and Mass Transfer, 1993. **36**(8): p. 2083-2092.

10. Abhat, A., *Low-Temperature Latent-Heat Thermal-Energy Storage - Heat-Storage Materials.* Solar Energy, 1983. **30**(4): p. 313-332.
11. Sodhi, G.S., K. Vigneshwaran, and P. Muthukumar, *Experimental investigations of high-temperature shell and multi-tube latent heat storage system.* Applied Thermal Engineering, 2021. **198**.
12. Beyne, W., et al., *A technical, financial and CO2 emission analysis of the implementation of metal foam in a thermal battery for cold chain transport.* Journal of Energy Storage, 2021. **35**.
13. Couvreur, K., et al., *Hot water storage for increased electricity production with organic Rankine cycle from intermittent residual heat sources in the steel industry.* Energy, 2020. **200**.
14. Couvreur, K., et al., *Constant power production with an organic Rankine cycle from a fluctuating waste heat source by using thermal storage*, in *Proceeding of the Heat Powered Cycles Conference*. 2018: Bayreuth, Germany.
15. Dumont, O., et al., *Carnot battery technology: A state-of-the-art review.* Journal of Energy Storage, 2020. **32**.
16. Castell, A. and C. Sole, *An overview on design methodologies for liquid-solid PCM storage systems.* Renewable & Sustainable Energy Reviews, 2015. **52**: p. 289-307.
17. Beyne, W., et al., *A charging time energy fraction method for evaluating the performance of a latent thermal energy storage heat exchanger.* Applied Thermal Engineering, 2021. **195**.
18. Zalba, B., et al., *Review on thermal energy storage with phase change: materials, heat transfer analysis and applications.* Applied Thermal Engineering, 2003. **23**(3): p. 251-283.
19. Fan, L.W. and J.M. Khodadadi, *Thermal conductivity enhancement of phase change materials for thermal energy storage: A review.* Renewable & Sustainable Energy Reviews, 2011. **15**(1): p. 24-46.
20. Faraj, K., et al., *Phase change material thermal energy storage systems for cooling applications in buildings: A review.* Renewable & Sustainable Energy Reviews, 2020. **119**.
21. Oro, E., et al., *Review on phase change materials (PCMs) for cold thermal energy storage applications.* Applied Energy, 2012. **99**: p. 513-533.
22. Gasia, J., L. Miro, and L.F. Cabeza, *Materials and system requirements of high temperature thermal energy storage systems: A review. Part 2: Thermal conductivity enhancement techniques.* Renewable & Sustainable Energy Reviews, 2016. **60**: p. 1584-1601.
23. Liu, M., W. Saman, and F. Bruno, *Review on storage materials and thermal performance enhancement techniques for high temperature phase change thermal storage systems.* Renewable & Sustainable Energy Reviews, 2012. **16**(4): p. 2118-2132.
24. Jegadheeswaran, S. and S.D. Pohekar, *Performance enhancement in latent heat thermal storage system: A review.* Renewable & Sustainable Energy Reviews, 2009. **13**(9): p. 2225-2244.
25. Sciacovelli, A., F. Colella, and V. Verda, *Melting of PCM in a thermal energy storage unit: Numerical investigation and effect of nanoparticle enhancement.* International Journal of Energy Research, 2013. **37**(13): p. 1610-1623.
26. Mahdi, J.M., S. Lohrasbi, and E.C. Nsofor, *Hybrid heat transfer enhancement for latent-heat thermal energy storage systems: A review.* International Journal of Heat and Mass Transfer, 2019. **137**: p. 630-649.
27. Sciacovelli, A., F. Gagliardi, and V. Verda, *Maximization of performance of a PCM latent heat storage system with innovative fins.* Applied Energy, 2015. **137**: p. 707-715.
28. Zhang, S.Q., et al., *Melting performance analysis of phase change materials in different finned thermal energy storage.* Applied Thermal Engineering, 2020. **176**.
29. Duan, J., Y.L. Xiong, and D. Yang, *Study on the effect of multiple spiral fins for improved phase change process.* Applied Thermal Engineering, 2020. **169**.
30. Mehta, D.S., et al., *Thermal performance augmentation in latent heat storage unit using spiral fin: An experimental analysis.* Journal of Energy Storage, 2020. **31**.

31. Lu, B.H., et al., *Experimental investigation on thermal behavior of paraffin in a vertical shell and spiral fin tube latent heat thermal energy storage unit.* Applied Thermal Engineering, 2021. **187**.
32. Johnson, M., et al., *High temperature latent heat thermal energy storage integration in a co-gen plant.* 9th International Renewable Energy Storage Conference, Ires 2015, 2015. **73**: p. 281-288.
33. Johnson, M., et al., *Design of high temperature thermal energy storage for high power levels.* Sustainable Cities and Society, 2017. **35**: p. 758-763.
34. Zhang, C.B., J. Li, and Y.P. Chen, *Improving the energy discharging performance of a latent heat storage (LHS) unit using fractal-tree-shaped fins.* Applied Energy, 2020. **259**.
35. Sheikholeslami, M., S. Lohrasbi, and D.D. Ganji, *Response surface method optimization of innovative fin structure for expediting discharging process in latent heat thermal energy storage system containing nano-enhanced phase change material.* Journal of the Taiwan Institute of Chemical Engineers, 2016. **67**: p. 115-125.
36. Sheikholeslami, M., S. Lohrasbi, and D.D. Ganji, *Numerical analysis of discharging process acceleration in LHTESS by immersing innovative fin configuration using finite element method.* Applied Thermal Engineering, 2016. **107**: p. 154-166.
37. Wu, L.Y., X. Zhang, and X.D. Liu, *Numerical analysis and improvement of the thermal performance in a latent heat thermal energy storage device with spiderweb-like fins.* Journal of Energy Storage, 2020. **32**.
38. Modi, N., et al., *Melting characteristics of a longitudinally finned-tube horizontal latent heat thermal energy storage system.* Solar Energy, 2021. **230**: p. 333-344.
39. Mao, Q., X. Hu, and T. Li, *Study on heat storage performance of a novel vertical shell and multi-finned tube tank.* Renewable Energy, 2022. **193**: p. 13.
40. Yang, X.H., et al., *Effect of fin number on the melting phase change in a horizontal finned shell-and-tube thermal energy storage unit.* Solar Energy Materials and Solar Cells, 2022. **236**.
41. Yang, X.H., et al., *Design of non-uniformly distributed annular fins for a shell-and-tube thermal energy storage unit.* Applied Energy, 2020. **279**.
42. Zhu, Y.X. and Y. Qiu, *Annular variable-spacing fin arrangement in latent heat storage system.* Journal of Energy Storage, 2022. **50**.
43. Guo, J.F., et al., *Melting assessment on the angled fin design for a novel latent heat thermal energy storage tube.* Renewable Energy, 2022. **183**: p. 406-422.
44. Kalapala, L. and J.K. Devanuri, *Influence of Fin Parameters on Melting and Solidification Characteristics of a Conical Shell and Tube Latent Heat Storage Unit.* Journal of Energy Resources Technology-Transactions of the Asme, 2022. **144**(2).
45. Ghani, F., et al., *Non-linear system identification of a latent heat thermal energy storage system.* Applied Thermal Engineering, 2018. **134**: p. 585-593.
46. Turkyilmazoglu, M., *Stefan problems for moving phase change materials and multiple solutions.* International Journal of Thermal Sciences, 2018. **126**: p. 67-73.
47. Groulx, D., A. Castell, and C. Solé, *11 - Design of latent heat energy storage systems using phase change materials*, in *Advances in Thermal Energy Storage Systems (Second Edition)*, L.E. Cabeza, Editor. 2021, Woodhead Publishing. p. 331-357.
48. Kim, M.H., et al., *New effective thermal conductivity model for the analysis of whole thermal storage tank.* International Journal of Heat and Mass Transfer, 2019. **131**: p. 1109-1116.
49. Shatikian, V., G. Ziskind, and R. Letan, *Transient performance of a finned PCM heat sink.* Ht2005: Proceedings of the Asme Summer Heat Transfer Conference 2005, Vol 2, 2005: p. 873-878.
50. Stritih, U., *An experimental study of enhanced heat transfer in rectangular PCM thermal storage.* International Journal of Heat and Mass Transfer, 2004. **47**(12-13): p. 2841-2847.

51. Ogoh, W. and D. Groulx, *Effects of the number and distribution of fins on the storage characteristics of a cylindrical latent heat energy storage system: a numerical study.* Heat and Mass Transfer, 2012. **48**(10): p. 1825-1835.
52. Hasan, A., *Phase-Change Material Energy-Storage System Employing Palmitic Acid.* Solar Energy, 1994. **52**(2): p. 143-154.
53. Tian, Y., et al., *Bionic topology optimization of fins for rapid latent heat thermal energy storage.* Applied Thermal Engineering, 2021. **194**.
54. Yang, X.H., et al., *Thermal performance of a shell-and-tube latent heat thermal energy storage unit: Role of annular fins.* Applied Energy, 2017. **202**: p. 558-570.
55. Abdulateef, A.M., et al., *Geometric and design parameters of fins employed for enhancing thermal energy storage systems: a review.* Renewable & Sustainable Energy Reviews, 2018. **82**: p. 1620-1635.
56. Pandey, S., et al., *A numerical investigation of the effect of fin inclination angle on the thermal energy storage performance of a phase change material in a rectangular latent heat thermal energy storage unit.* Journal of Energy Storage, 2022. **47**.
57. Verma, P., Varun, and S.K. Singal, *Review of mathematical modeling on latent heat thermal energy storage systems using phase-change material.* Renewable & Sustainable Energy Reviews, 2008. **12**(4): p. 999-1031.
58. Al-abidi, A.A., et al., *CFD applications for latent heat thermal energy storage: a review.* Renewable & Sustainable Energy Reviews, 2013. **20**: p. 353-363.
59. Dutil, Y., et al., *A review on phase-change materials: Mathematical modeling and simulations.* Renewable & Sustainable Energy Reviews, 2011. **15**(1): p. 112-130.
60. Trp, A., *An experimental and numerical investigation of heat transfer during technical grade paraffin melting and solidification in a shell-and-tube latent thermal energy storage unit.* Solar Energy, 2005. **79**(6): p. 648-660.
61. Beyne, W., et al., *Estimating the state of charge in a latent thermal energy storage heat exchanger based on inlet/outlet and surface measurements.* Applied Thermal Engineering, 2022. **201**.
62. Vogel, J. and M. Johnson, *Natural convection during melting in vertical finned tube latent thermal energy storage systems.* Applied Energy, 2019. **246**: p. 38-52.
63. Shmueli, H., G. Ziskind, and R. Letan, *Melting in a vertical cylindrical tube: Numerical investigation and comparison with experiments.* International Journal of Heat and Mass Transfer, 2010. **53**(19-20): p. 4082-4091.
64. Kumar, M. and D.J. Krishna, *Influence of Mushy Zone Constant on Thermohydraulics of a PCM.* International Conference on Recent Advancement in Air Conditioning and Refrigeration, Raar 2016, 2017. **109**: p. 314-321.
65. Park, S.H., Y.G. Park, and M.Y. Ha, *A numerical study on the effect of the number and arrangement of tubes on the melting performance of phase change material in a multi-tube latent thermal energy storage system.* Journal of Energy Storage, 2020. **32**.
66. Arena, S., et al., *Numerical simulation of a finned-tube LHTES system: influence of the mushy zone constant on the phase change behaviour.* Ati 2017 - 72nd Conference of the Italian Thermal Machines Engineering Association, 2017. **126**: p. 517-524.
67. Tehrani, S.S.M., et al., *An improved, generalized effective thermal conductivity method for rapid design of high temperature shell-and-tube latent heat thermal energy storage systems.* Renewable Energy, 2019. **132**: p. 694-708.
68. Huisseune, H., et al., *Comparison of metal foam heat exchangers to a finned heat exchanger for low Reynolds number applications.* International Journal of Heat and Mass Transfer, 2015. **89**: p. 1-9.
69. Huisseune, H., et al., *Performance enhancement of a louvered fin heat exchanger by using delta winglet vortex generators.* International Journal of Heat and Mass Transfer, 2013. **56**(1-2): p. 475-487.

70. Kakaç, S., H. Liu, and A. Pramuanjaroenkij, *Heat exchangers : selection, rating, and thermal design*. Fourth edition ed. 2020, Boca Raton: CRC Press.
71. Aghbalou, F., F. Badia, and J. Illa, *Exergetic optimization of solar collector and thermal energy storage system.* International Journal of Heat and Mass Transfer, 2006. **49**(7-8): p. 1255-1263.
72. Fang, Y.H., J.L. Niu, and S.M. Deng, *An analytical technique for the optimal designs of tube-in-tank thermal energy storage systems using PCM.* International Journal of Heat and Mass Transfer, 2019. **128**: p. 849-859.
73. Tay, N.H.S., et al., *An effectiveness-NTU technique for characterising a finned tubes PCM system using a CFD model.* Applied Energy, 2014. **131**: p. 377-385.
74. Zhao, C.R., et al., *Review of analytical studies of melting rate enhancement with fin and/or foam inserts.* Applied Thermal Engineering, 2022. **207**.
75. Bechiri, M. and K. Mansouri, *Analytical solution of heat transfer in a shell-and-tube latent thermal energy storage system.* Renewable Energy, 2015. **74**: p. 825-838.
76. Mostafavi, A., M. Parhizi, and A. Jain, *Semi-analytical thermal modeling of transverse and longitudinal fins in a cylindrical phase change energy storage system.* International Journal of Thermal Sciences, 2020. **153**.
77. Lamberg, P. and K. Siren, *Analytical model for melting in a semi-infinite PCM storage with an internal fin.* Heat and Mass Transfer, 2003. **39**(2): p. 167-176.
78. Rozenfeld, T., et al., *Close-contact melting in a horizontal cylindrical enclosure with longitudinal plate fins: Demonstration, modeling and application to thermal storage.* International Journal of Heat and Mass Transfer, 2015. **86**: p. 465-477.
79. Lorente, S., A. Bejan, and J.L. Niu, *Phase change heat storage in an enclosure with vertical pipe in the center.* International Journal of Heat and Mass Transfer, 2014. **72**: p. 329-335.
80. Mosaffa, A.H., et al., *Approximate analytical model for PCM solidification in a rectangular finned container with convective cooling boundaries.* International Communications in Heat and Mass Transfer, 2012. **39**(2): p. 318-324.
81. Bauer, T., *Approximate analytical solutions for the solidification of PCMs in fin geometries using effective thermophysical properties.* International Journal of Heat and Mass Transfer, 2011. **54**(23-24): p. 4923-4930.
82. Tarragona, J., et al., *Experimental analysis of a latent thermal energy storage system enhanced with metal foam.* Journal of Energy Storage, 2021. **41**.
83. Fornarelli, F., S.M. Camporeale, and B. Fortunato, *Simplified theoretical model to predict the melting time of a shell-and-tube LHTES.* Applied Thermal Engineering, 2019. **153**: p. 51-57.
84. Manish, K.R. and B. Jyotirmay, *Development of correlation for melting time of phase change material in latent heat storage unit.* Clean, Efficient and Affordable Energy for a Sustainable Future, 2015. **75**: p. 2125-2130.
85. Duan, J., Y.L. Xiong, and D. Yang, *On the Melting Process of the Phase Change Material in Horizontal Rectangular Enclosures.* Energies, 2019. **12**(16).
86. Diarce, G., et al., *A novel correlation for the direct determination of the discharging time of plate-based latent heat thermal energy storage systems.* Applied Thermal Engineering, 2018. **129**: p. 521-534.
87. Waser, R., et al., *Fast and experimentally validated model of a latent thermal energy storage device for system level simulations.* Applied Energy, 2018. **231**: p. 116-126.
88. Bauer, D., D. Laing, and R. Tamme, *Overview of PCMs for Concentrated Solar Power in the Temperature Range 200 to 350°C.* Advances in Science and Technology, 2010. **74**: p. 272-277.
89. Agyenim, F., P. Eames, and M. Smyth, *Heat transfer enhancement in medium temperature thermal energy storage system using a multitube heat transfer array.* Renewable Energy, 2010. **35**(1): p. 198-207.

90. Yang, L.Z., et al., *Shell-and-Tube Latent Heat Thermal Energy Storage Design Methodology with Material Selection, Storage Performance Evaluation, and Cost Minimization.* Applied Sciences-Basel, 2021. **11**(9).
91. Agyenim, F., et al., *A review of materials, heat transfer and phase change problem formulation for latent heat thermal energy storage systems (LHTESS).* Renewable & Sustainable Energy Reviews, 2010. **14**(2): p. 615-628.
92. Lecompte, S., et al., *Experimental results of a small-scale organic Rankine cycle: Steady state identification and application to off-design model validation.* Applied Energy, 2018. **226**: p. 82-106.
93. Seddegh, S., et al., *Comparison of heat transfer between cylindrical and conical vertical shell-and-tube latent heat thermal energy storage systems.* Applied Thermal Engineering, 2018. **130**: p. 1349-1362.
94. Seddegh, S., et al., *Investigation of the effect of geometric and operating parameters on thermal behavior of vertical shell-and-tube latent heat energy storage systems.* Energy, 2017. **137**: p. 69-82.
95. Tamme, R., et al., *Latent heat storage above 120 degrees C for applications in the industrial process heat sector and solar power generation.* International Journal of Energy Research, 2008. **32**(3): p. 264-271.
96. Orozco, M.A., et al., *Thermal Storage of Nitrate Salts as Phase Change Materials (PCMs).* Materials, 2021. **14**(23).
97. D'Aguanno, B., et al., *Thermostatic properties of nitrate molten salts and their solar and eutectic mixtures.* Scientific Reports, 2018. **8**.
98. Mohamed, S.A., et al., *A review on current status and challenges of inorganic phase change materials for thermal energy storage systems.* Renewable & Sustainable Energy Reviews, 2017. **70**: p. 1072-1089.
99. Vogel, J., M. Keller, and M. Johnson, *Numerical modeling of large-scale finned tube latent thermal energy storage systems.* Journal of Energy Storage, 2020. **29**.
100. Barz, T., et al., *Experimental Analysis and Numerical Modeling of a Shell and Tube Heat Storage Unit with Phase Change Materials.* Industrial & Engineering Chemistry Research, 2016. **55**(29): p. 8154-8164.
101. Joybari, M.M., et al., *Experimental investigation of multiple tube heat transfer enhancement in a vertical cylindrical latent heat thermal energy storage system.* Renewable Energy, 2019. **140**: p. 234-244.
102. Bell, I.H., et al., *Pure and Pseudo-pure Fluid Thermophysical Property Evaluation and the Open-Source Thermophysical Property Library CoolProp.* Industrial & Engineering Chemistry Research, 2014. **53**(6): p. 2498-2508.
103. VDI-Gesellschaft Verfahrenstechnik und Chemieingenieurwesen., *VDI heat atlas*. 2nd ed. VDI-buch. 2010, Berlin ; New York: Springer. xxi, 1585 p.
104. Gnielinski, V., *On heat transfer in tubes.* International Journal of Heat and Mass Transfer, 2013. **63**: p. 134-140.
105. Gnielinski, V., *On heat transfer in tubes (vol 63, pg 134, 2013).* International Journal of Heat and Mass Transfer, 2015. **81**: p. 638-638.
106. Jmal, I. and M. Baccar, *Numerical study of PCM solidification in a finned tube thermal storage including natural convection.* Applied Thermal Engineering, 2015. **84**: p. 320-330.
107. Tehrani, S.S.M., G. Diarce, and R.A. Taylor, *The error of neglecting natural convection in high temperature vertical shell-and-tube latent heat thermal energy storage systems.* Solar Energy, 2018. **174**: p. 489-501.
108. Liu, Z.Y., Y.P. Yao, and H.Y. Wu, *Numerical modeling for solid-liquid phase change phenomena in porous media: Shell-and-tube type latent heat thermal energy storage.* Applied Energy, 2013. **112**: p. 1222-1232.

109. Tao, Y.B. and Y.L. He, *Numerical study on thermal energy storage performance of phase change material under non-steady-state inlet boundary.* Applied Energy, 2011. **88**(11): p. 4172-4179.
110. Farid, M.M., F.A. Hamad, and M. Abu-Arabi, *Melting and solidification in multi-dimensional geometry and presence of more than one interface.* Energy Conversion and Management, 1998. **39**(8): p. 809-818.
111. Yang, H.T. and Y.Q. He, *Solving heat transfer problems with phase change via smoothed effective heat capacity and element-free Galerkin methods.* International Communications in Heat and Mass Transfer, 2010. **37**(4): p. 385-392.
112. Cui, M., et al., *Numerical solution of phase change heat transfer problems by effective heat capacity model and element differential method.* Journal of Computational Science, 2022. **60**.
113. Yao, W.A., et al., *Precise integration boundary element method for solving dual phase change problems based on the effective heat capacity model.* Engineering Analysis with Boundary Elements, 2019. **108**: p. 411-421.
114. Prasad, J.S., et al., *Comparative study of phase change phenomenon in high temperature cascade latent heat energy storage system using conduction and conduction-convection models.* Solar Energy, 2018. **176**: p. 627-637.
115. Virtanen, P., et al., *SciPy 1.0: fundamental algorithms for scientific computing in Python.* Nature Methods, 2020. **17**(3): p. 261-272.
116. Roache, P.J., *Quantification of Uncertainty in Computational Fluid Dynamics.* Annual Review of Fluid Mechanics, 1997. **29**(1): p. 123-160.
117. Roache, P.J., *Quantification of uncertainty in computational fluid dynamics.* Annual Review of Fluid Mechanics, 1997. **29**: p. 123-160.

Appendix A: PDF parameters of the apparent heat capacity

In the normal distribution function, $\phi(T_{PCM})$, the mean of the distribution μ is the location parameter and $\frac{T_{mlt,u}+T_{mlt,l}}{2}$ is used. The standard deviation, σ represents the scale parameter and $\frac{T_{mlt,u}-T_{mlt,l}}{6}$ is used which corresponds to 99.7% of the area beneath the curve for $T_{mlt,l} < T_{PCM} < T_{mlt,u}$. This means that there is an offset of the curve, c if $T_{PCM} = \{T_{mlt,l}, T_{mlt,u}\}$ which should be eliminated. Only the area beneath the normal distribution with offset elimination is equal to latent heat. This results to Eq. 55, where $c_{p,ND}$ is the heat capacity of the normal distribution with offset elimination. This constraint yields the requirement for a multiplication factor for the normal distribution, b.

$$h_{PCM} = \int_{T_{mlt,l}}^{T_{mlt,l}} c_{p,ND}(T_{PCM})dT \qquad 55$$

Appendix B: Grid convergence of the finite volume model

The model is discretized in two dimensions with n_x the number of control volumes in the flow direction and n_y the number of control volumes in the radial direction. The grid convergence is checked using the method of Roache [117].

A coarse grid Richardson error estimator is used in which the error in a coarse grid solution, f_2 is compared to the solution of a fine grid, f_1. To account for the uncertainty in the Richardson error estimator a safety factor of 1.25 is used to give the grid convergence index (GCI) as in Eq. 56.

$$GCI_{coarse} = 1.25 \left| \frac{r^p \varepsilon}{1 - r^p} \right| \qquad 56$$

With ε the difference of a selected parameter between the coarse grid solution and the fine grid solution ($\varepsilon = f_2 - f_1$). p is the formal order of accuracy of the algorithm. If the grid refinement is performed with constant grid refinement ratio, r then this order of accuracy, p can be derived as Eq. 57.

$$p = \frac{\ln\left(\frac{f_3 - f_2}{f_2 - f_1}\right)}{\ln(r)} \quad 57$$

With subscript 1 indicating the finest grid, subscript 3 the coarsest grid and subscript 2 a grid between the finest and the coarsest.

Firstly, the grid convergence is checked for HTF outlet temperature, T_{out} and the melt fraction, α_m for test 1 (see Section 3). A grid independence test has been done in two steps. In the first step, the grid convergence along the *x* and *y* direction are checked separately by comparing results for n_x = 15, 30 and 60 with the other direction fixed at n_y = 5 and for n_y = 5, 10 and 20 with the other direction fixed at n_x = 15. In the second step the grid convergence is checked in both directions with grids of (n_x = 15, n_y=5) , (n_x=30, n_y=10) and (n_x=60,n_y=20). 2000 timesteps have been chosen resulting in a fixed timestep of 7.83 s. There is no significant change in the results when the grid size is changed.

Secondly, to fix the time step for solving the governing equations, a time independence test is carried out. The time-wise variation of the HTF outlet temperature and the melt fraction has been checked for three timesteps: 1.96 s, 3.92 s, and 7.83 s for the coarse grid (n_x = 15, n_y = 5). This corresponds to a number of timesteps, *Nts,* of respectively 8000, 4000, 2000. There is no significant fluctuation in the results as the timestep reduces from 7.83 to 1.96 s. Considering the grid independence test and the time independence test, the grid size of (n_x = 15, n_y = 5) with a time step of 1 s is chosen for all simulations. The results of the grid and time independence tests are summarized in Table 8 and Figure 22.

Table 8. Results of the grid convergence tests. Results are given for the HTF outlet temperature and the melt fraction, α_m.

	ε_{21}	ε_{32}	p	GCI_{21} [°C]	GCI_{32} [°C]
n_x (T_{out})	0.064	0.12	0.96	0.17	0.32
n_x (α_m)	0.00031	0.00056	0.86	0.00087	0.0016
n_y (T_{out})	0.038	0.042	0.16	0.46	0.51
n_y(α_m)	0.0018	0.0032	0.87	0.0048	0.0089
2D (T_{out})	0.067	0.13	1.00	0.17	0.33
2D (α_m)	0.0017	0.0037	1.15	0.0038	0.085
Nts (T_{out})	0.004	0.006	0.49	0.018	0.025
Nts (α_m)	6.16E-5	0.00011	0.80	0.00018	0.00032

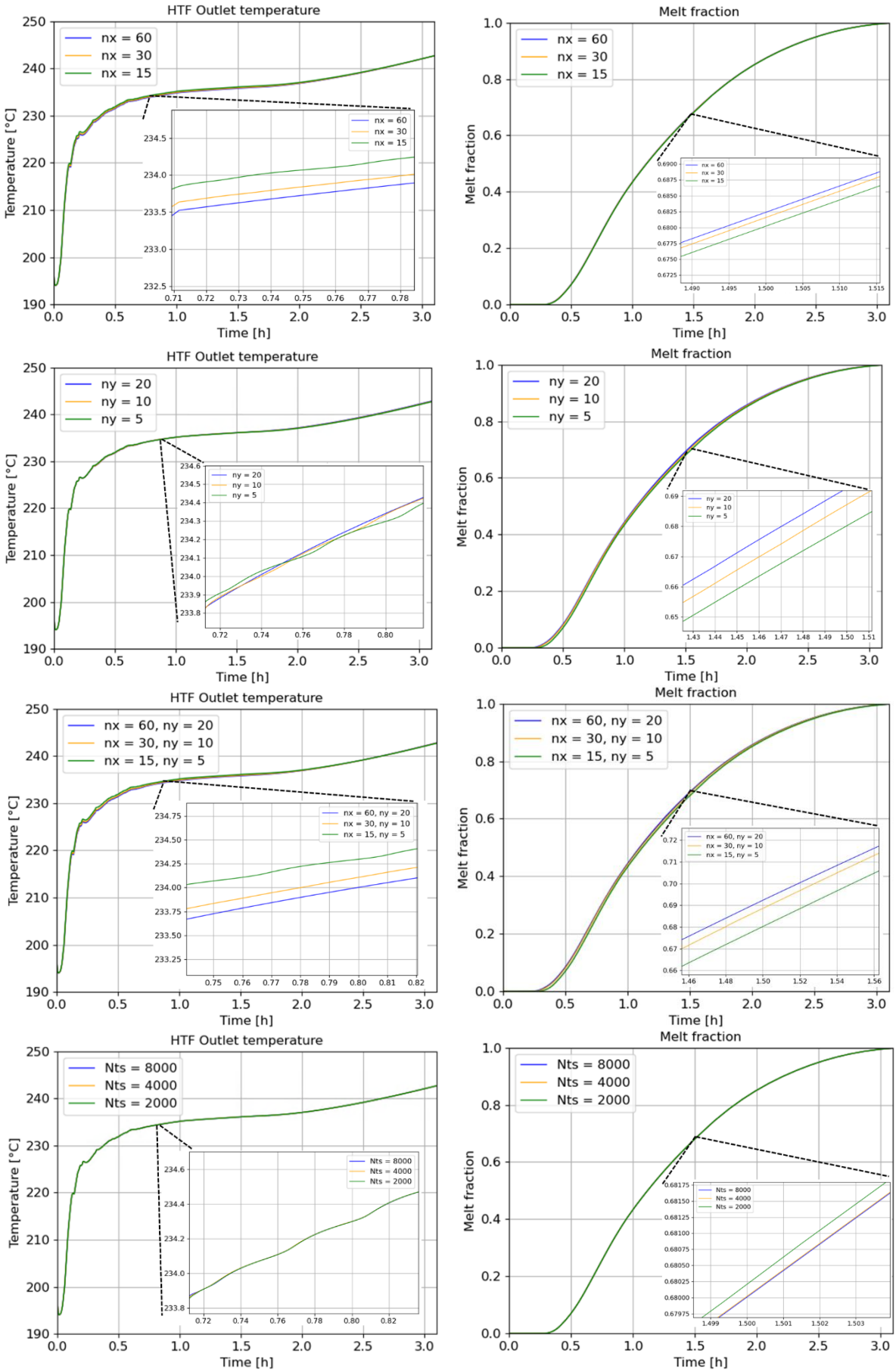

Figure 22. Results of the grid independence tests.

Nomenclature

Roman symbols

A	Area	[m²]
c	Specific heat capacity	[J/kgK]
$\tilde{c}_p$	Apparent specific heat capacity	[J/kgK]
d_i	Tube inner diameter	[m]
F	Integrated efflux of energy	[J]
$\dot{F}$	Efflux of energy	[W]
h	Specific enthalpy	[J/kg]
h_c	Convective heat transfer coefficient	[W/m²K]
$I_{\Delta T}$	Integrated absolute temperature difference	[K]
J	Stored internal energy	[J]
k	Thermal conductivity	[W/mK]
k_{eff}	Effective thermal conductivity	[W/mK]
m	Mass	[kg]
$\dot{m}$	Mass flow rate	[kg/s]
n	Power factor	[-]
Nts	Number of timesteps	[-]
N_{tubes}	Number of HTF tubes in the LTES unit	[-]
n_x	Number of control volumes in the HTF flow direction	[-]
n_y	Number of PCM control volumes in the radial direction	[-]
Nu	Nusselt number	[-]
p	Order of convergence	[-]
Pr	Prandtl number	[-]
$\dot{Q}$	Heat transfer rate	[W]
Q	Heat energy	[J]
R	Thermal resistance	[K/W]
Re	Reynolds number	[-]
t	Time	[s]
t_c	Charging time	[s]
T	Temperature	[°C]
U	Internal energy	[J]
UA	Overall heat transfer coefficient	[W/K]
x	Distance from inlet of the tube	[m]
$\vec{x}$	Location	[m,m,m]
Z	Total error between experiment and finite volume simulation	[-]

Greek symbols

α	Energy fraction	[-]
λ	Liquid fraction	[-]
Δ	Difference	[-]

Acronyms

CFD	Computational Fluid Dynamics	
CTEFM	Charging Time Energy Fraction Method	
GCI	Grid Convergence Index	[K]
HTF	Heat Transfer Fluid	
LTES	Latent Thermal Energy Storage	
ODE	Ordinary Differential Equation	
ORC	Organic Rankine Cycle	

PCM	Phase Change Materials
PDF	Probability Distribution Function
PLC	Programmable Logic Controller
FV	Finite volume

Scripts

amb	Ambient
c	Charging time energy fraction method experiment
cont	container
cor	correlation
end	End of the charging cycle
exp	experiment
f	Finite volume experiment
htf	Heat transfer fluid
i	Index in time or space or experiment
in	Inlet of the heat transfer fluid
ini	Initial
j	Index in time or space or experiment
l	Liquid
loss	Heat losses
max	maximum
mlt	Melting
out	Outlet of the heat transfer fluid
s	solid
sim	simulation
Surf,1	Surface between PCM and insulation
start	Start of the charging cycle